AGU PUBLICATIONS

JGR

Journal of Geophysical Research: Solid Earth

RESEARCH ARTICLE
10.1002/2016JB013374

Key Points:
- Brazilian tests with DIC reveal the tensile strain of Mancos Shale due to anisotropic microlithofacies and mineralogical heterogeneity
- Phase-field modeling results show that spatial heterogeneity and material anisotropy highly affect crack patterns and effective fracture toughness
- Crack coalescence and interaction mechanisms using two-constituent models explain the wide spectrum of effective toughness of shale observed in the literature

Supporting Information:
- Supporting Information S1

Correspondence to:
H. Yoon,
hyoon@sandia.gov

Citation:
Na S. H., W. C. Sun, M. D. Ingraham, and H. Yoon (2017), Effects of spatial heterogeneity and material anisotropy on the fracture pattern and macroscopic effective toughness of Mancos Shale in Brazilian tests, *J. Geophys. Res. Solid Earth*, *122*, doi:10.1002/2016JB013374.

Received 18 JUL 2016
Accepted 28 JUL 2017
Accepted article online 31 JUL 2017

Effects of spatial heterogeneity and material anisotropy on the fracture pattern and macroscopic effective toughness of Mancos Shale in Brazilian tests

SeonHong Na[1], WaiChing Sun[1], Mathew D. Ingraham[2], and Hongkyu Yoon[2]

[1]Department of Civil Engineering and Engineering Mechanics, Columbia University, New York, New York, USA, [2]Geomechanics Department, Sandia National Laboratories, Albuquerque, New Mexico, USA

Abstract For assessing energy-related activities in the subsurface, it is important to investigate the impact of the spatial variability and anisotropy on the geomechanical behavior of shale. The Brazilian test, an indirect tensile-splitting method, is performed in this work, and the evolution of strain field is obtained using digital image correlation. Experimental results show the significant impact of local heterogeneity and lamination on the crack pattern characteristics. For numerical simulations, a phase field method is used to simulate the brittle fracture behavior under various Brazilian test conditions. In this study, shale is assumed to consist of two constituents including the stiff and soft layers to which the same toughness but different elastic moduli are assigned. Microstructural heterogeneity is simplified to represent mesoscale (e.g., millimeter scale) features such as layer orientation, thickness, volume fraction, and defects. The effect of these structural attributes on the onset, propagation, and coalescence of cracks is explored. The simulation results show that spatial heterogeneity and material anisotropy highly affect crack patterns and effective fracture toughness, and the elastic contrast of two constituents significantly alters the effective toughness. However, the complex crack patterns observed in the experiments cannot completely be accounted for by either an isotropic or transversely isotropic effective medium approach. This implies that cracks developed in the layered system may coalesce in complicated ways depending on the local heterogeneity, and the interaction mechanisms between the cracks using two-constituent systems may explain the wide range of effective toughness of shale reported in the literature.

Plain Language Summary Shale has become increasingly important for emerging energy technology problems in the subsurface such as unconventional gas and oil recovery, geologic storage of CO2, enhanced oil recovery, and nuclear waste disposal. In particular, geomechanical behavior of shale rocks is important to assess crack initiation and propagation which can be important for energy-related activities including fluid injection/extraction and fracturing. In this work, an indirect tensile test on Mancos Shale was performed, and the evolution of the strain field and growth of the fractures were experimentally obtained using digital imaging process. Experimental results reveal the significant impact of small features and laminations on the characterization of crack patterns. Based on the experimental observations, numerical modeling has been conducted to simulate fracture processes under various conditions mimicking the experimental setup. Simulation results show that spatial heterogeneity and material anisotropy reflecting microstructural attributes highly affect crack patterns and effective fracture toughness, and the contrast of elasticity of the two constituents (stiff and soft materials) was sufficient to significantly alter the effective toughness. Overall, this work provides a robust workflow to explain the wide spectrum of effective toughness of shale reported in the literature.

1. Introduction

Subsurface energy-related activities including hydraulic fracturing and geological carbon storage are significantly influenced by the geomechanical behavior of shale. Predicting the onset and propagation of brittle fracture in shale is important to evaluate the mechanical behavior of shale. Shales are strongly anisotropic and heterogeneous, and fracture initiation and propagation in shale depend on the interaction between anisotropic mechanical properties and in situ stress conditions [*Chandler et al.*, 2016]. In particular, the compositional and structural features of very fine sedimentary rocks may significantly affect brittle fracture behaviors of shale. To be specific, the presence of platy clay minerals and compliant organic materials in shale significantly influences the spatial microheterogeneity in the layered system [*Amadei*, 1996; *Heath et al.*, 2012;

Loucks et al., 2012; *Hart et al*., 2013]. In addition, the anisotropy of shale is often attributed to many factors including sedimentary bedding layers, irregular features, and mineralogical orientation [e.g., *Kaarsberg*, 1959; *Cholach and Schmitt*, 2006; *Sondergeld and Rai*, 2011; *Ong et al*., 2016]. Lamination with defects or gaps may also lead to a more complex crack path, affecting the measured effective strength and toughness of the shale formation. Clays and organics are weak components of shale that create weak links between stronger components (e.g., cements along grains). To represent the mechanical properties of a strongly layered sedimentary system, a two-constituent composite consisting of the soft (e.g., clays and organics) and stiff (e.g., quartz and calcite) components can be conceptually used as a surrogate system for shale [*Vernik and Nur*, 1992; *Vernik and Liu*, 1997; *Sone and Zoback*, 2013a, 2013b].

For layered composite materials, the effective medium approach has been employed to represent the heterogeneous layered material as a macroscopic effective medium [*Gray et al*., 2009; *Lenoir et al*., 2010; *Sun et al*., 2011a, 2011b, 2013]. For example, *Backus* [1962] presents a method producing the effective constants for a finely layered medium composed of either isotropic or anisotropic elastic layers [e.g., *Berryman*, 1998]. While the isotropic simplification in the effective medium approach might be acceptable for materials with very weak anisotropy, this method is ineffective for interpreting the material properties with strongly preferred orientations. Recent work by *Hossain et al*. [2014] shows that the spatial distribution of the constituents with different elastic properties can significantly impact effective fracture toughness, even when the toughness of each constituent is similar or identical. In addition to the anisotropy that originates from mineralogical bedding layers, the fact that spatial distribution of constituents can affect shale's behavior prompted us to analyze how the elastic anisotropy alters the brittle fracture of shale.

Experimentally, crack growth inside a shale specimen is strongly influenced by the loading angle with respect to the bedding planes, the distribution of micropores, and the defects of the layered structures [*Tavallali and Vervoort*, 2010a, 2013; *Simpson*, 2013; *Chandler et al*., 2016]. The onset and propagation of cracks in shale are predominated by the Mode I fracture with different amount of shear depending on the microheterogeneity and anisotropy of the bedding layers [*Chong et al*., 1984]. The Brazilian test, a simple indirect method of determining the tensile strength and effective fracture toughness of brittle materials, has been used for over 70 years [e.g., *Fairhurst*, 1964; *International Society of Rock Mechanics*, 1978; *Guo et al*., 1993]. Several experimental works have justified the practical use of the Brazilian test by demonstrating that a majority of rocks undergo a tensile failure in the biaxial condition (i.e., negligible intermediate principal stress) with the compressive stress less than three times the tensile stress. Popular for its simplicity and ease of setup, the Brazilian test, as a valid tensile testing method, has been debated. For example, *Fairhurst* [1964] evaluated the validity of the Brazilian test for rocks and rock-like materials by generalizing the Griffith failure criterion of the brittle materials. It was concluded that the fracture may not start from the disc center in the case of small angles of disc loading on the materials, invalidating the Brazilian tension test. *Perras and Diederichs* [2014] also state that invalid Brazilian tests can occur in sedimentary specimen due to the fabric plane and the effect of loading platen. Comprehensive review of experimental, analytical, and numerical studies of the Brazilian test has been reported [e.g., *Andreev*, 1991a, 1991b; *Li and Wong*, 2013; *Perras and Diederichs*, 2014].

Despite the debate the Brazilian test coupled with a digital imaging and acoustic emission measurement is very useful for analyzing the influence of material heterogeneity on crack initiation and propagation [e.g., *Simpson*, 2013; *Mighani et al*., 2014; *Wang et al*., 2016; *Mighani et al*., 2016]. Furthermore, recent experiments have been performed to account for the effect of the anisotropy or layered system of rocks on tensile strength and crack patterns [e.g., *Tavallali and Vervoort*, 2010a, 2013; *Dan et al*., 2013; *Vervoort et al*., 2014]. Most recently, *Chandler et al*. [2016] conducted the Brazilian test together with a modified short-rod test and wave velocity measurements to obtain the tensile strengths, fracture toughness, and directional fracture propagations in the strongly laminated Mancos Shale (i.e., horizontally oriented bedding). They demonstrated that fracture toughness is much higher when the crack plane is perpendicular rather than parallel to the bedding.

In addition to experimental characterizations, analytical or numerical studies for the Brazilian test may also provide an essential tool to predict brittle behavior of materials. For homogeneous, isotropic, and linearly elastic materials, *Hondros* [1959] derived a complete stress solution when the load is distributed over finite arcs with diametral compression. The Hondros's method was extended by *Pinto* [1979] to determine elastic constants of anisotropic materials. However, this method applied only to specimens with known principal

directions. For the transversely isotropic material in a circular disc, *Exadaktylos and Kaklis* [2001] derived an explicit solution of stress and strain domain. In addition, a combination of analytical and experimental methods was presented to determine the tensile strength of transversely isotropic rocks by the Brazilian test [e.g., *Chen et al*., 1998]. For the anisotropic rock, *Claesson and Bohloli* [2002] derived and used the analytical solutions to determine tensile strength using intrinsic parameters such as elastic modulus for transversely isotropic material. Although these analytical methods may contribute to our understanding of stress and strain distribution during the Brazilian test, analytical methods cannot fully account for heterogeneous material properties and both crack initiation and propagation processes.

Therefore, to overcome analytical limitations, numerical methods have been used to simulate the stress distribution and/or crack initiation and propagation of (transversely) isotropic rocks for the Brazilian test (see *Li and Wong* [2013] for a brief review). For example, these numerical efforts include the displacement continuity for investigating the influence of the loading contact on the initiation and propagation of fractures [e.g., *Malan et al*., 1994], the boundary element method for evaluating the effect of the initiated cracks on stress distribution within isotropic rock samples [e.g., *Lanaro et al*., 2009], the finite element method for 3-D stress analysis to show size/shape effects under the Brazilian test [e.g., *Yu et al*., 2006], and for analyzing failure process of heterogeneous isotropic rocks under static/dynamic loading [e.g., *Zhu and Tang*, 2006]. Recently, the numerical methods have been extended to utilize the extended finite element method for simulating crack propagation in the cracked Brazilian disc [e.g., *Eftekhari et al*., 2015], the discrete element method for the mechanical behavior of transversely isotropic rocks using embedded smooth joints (e.g., *Park and Min* [2015] in 2-D and *Park et al*. [2016] in 3-D), and the hybrid finite element method-discrete element method for analyzing the influence of microscale heterogeneity and microcracks on the brittle fractures [e.g., *Mahabadi*, 2012] and for modeling the transition from continuum to discontinuum during fracturing process [e.g., *An et al*., 2016]. Overall, conventional finite element method often requires complicated algorithms to capture arbitrary crack propagation, branching, and coalescence. Meanwhile, the discrete mechanics often requires breakage of bonds to represent fracture. However, the discrete fracture approaches need sharp interfaces with complex evolving topologies and explicit heuristics to numerically replicate the propagation and interaction of rocks.

One promising approach to overcome these numerical issues is to use an implicit function to represent cracks. In particular, phase field fracture model allows treating a crack in a continuum media as a diffusive region with a given characteristic length, instead of an embedded discontinuity. The phase field evolution can be therefore captured in finite element model with a continuous displacement field. By incorporating the generalized brittle fracture theory into a variational framework [*Griffith*, 1921], the onset, propagation, and coalescence of fracture in a deforming brittle material can be simulated via solving a multifield initial boundary value problem with solid displacement ($\boldsymbol{u}$) and the phase field (φ) as the unknowns in the spatial domain [e.g., *Miehe et al*., 2010a; *Heister et al*., 2015]. Both solid displacement field and phase field are the explicit function of position within the body Ω. A variety of phase field models has been applied for many engineering applications in quasi-static and dynamic regimes [*Bourdin et al*., 2008; *Miehe et al*., 2010a; *Hofacker and Miehe*, 2012, 2013], ductile or brittle fractures [*Ambati et al*., 2015; *Verhoosel and Borst*, 2013], anisotropic surface energy fracture [*Li et al*., 2015], and fluid-filled fracture [*Wick et al*., 2015]. The phase field approach numerically replicates the Brazilian test effectively because it does not require the crack path to be predetermined or straight, and it can handle crack coalescence and branching relatively easily.

The overall objective of this work is to evaluate the effects of material anisotropy and spatially heterogeneous features of Mancos Shale on the fracture patterns and the macroscopic toughness via the Brazilian test and phase-field modeling. By using digital image correlation (DIC) to capture the displacement of shale specimens in the Brazilian test, we first obtained experimental results to analyze how the orientation of layers affects the peak loading and the fracture patterns of Mancos Shale specimens. Following the experimental results, we performed a comprehensive series of two-dimensional numerical simulations using an adaptive phase field finite element model for brittle fracture [cf. *Heister et al*., 2015]. In these numerical tests, we assume that shale comprises layers of stiff and soft materials and that the critical energy release rate G_c of both layers is identical. We further idealize the shale specimen as a simply layered composite, in which the microheterogeneity within each layer is neglected. By conducting simulations with the numerical specimen of different orientations, thickness, volume fractions, and continuities of stiff and soft layers, we analyze

how these structural attributes affect the onset, propagation, and coalescence of the cracks, and ultimately the effective bulk and crack energies of the idealized materials and their implications for real experiments.

In the following sections, we briefly describe the Mancos Shale used in this study (section 2.1) before detailing the experimental procedure, numerical model, and simulation scenarios (section 2). We report and compare both experimental and simulation results, highlighting key findings (section 3). Finally, we summarize the key findings and provide potential future works (section 4).

2. Materials and Methods

2.1. Mancos Shale

The Mancos Shale Formation, deposited along the steep margin of the Western Interior Seaway during most of the Cretaceous [*Kauffman et al*., 1984], has several members such as dark gray (and black) calcareous and noncalcareous shales and interbedded sandstones. It has various thicknesses in the San Juan Basin [*Landis et al*., 1973; *Ridgley et al*., 2013] and the Uinta and Piceance Basins [*Hettinger and Kirschbaum*, 2002]. The Cretaceous Mancos Shale consists of a variety of lithofacies (i.e., rocks deposited in a distinct depositional environment) and relatively thin sandier layers contained in the sealing source muds, which was considered to be a regional seal [*Shipton et al*., 2004]. Relatively thin sandier layers contained in the sealing source muds and extensive fracture networks have historically been the targets for resource development in these rocks. The Mancos Shale has moderate to low total organic carbon (TOC) (less than 2% in shelf marine system tracts and 2–5% in transgressive systems tracts). This formation is commonly thought to be a source rock with oil and gas potential within Cretaceous Interior Seaway basins [*Pasley et al*., 1991]. In this work, Mancos Shale samples for testing were taken from a large block with a low TOC (~40 cm in diameter and 13 cm in thickness, $<$1% TOC) that has been used for characterizing microlithofacies with a wide range of structural, mineralogical, mechanical, and compositional heterogeneities [*Yoon et al*., 2015; *Grigg*, 2016].

2.2. Brazilian Tests

Four cores of Mancos Shale consisting of two samples cored parallel to horizontal bedding and two samples cored perpendicular to the bedding were used for the Brazilian test. The cores have a size of ~26 mm in diameter and ~13 mm in thickness. The specimens were prepared and tested following the standard method *[American Society for Testing and Materials (ASTM)*, 2008]. The tests were performed on a 100 kN load frame equipped with a 10 kN load cell, and displacements were measured with a ±1.27 cm platen mounted extensometer. The specimens were compressed on the edge between a pair of the flat and parallel platens as seen in Figure 1. A single thickness of masking tape wrapped the specimen to reduce the stress concentration at the loading points as well as to contain the specimen after failure. Maintaining the specimen relatively intact helps confirm the fracture pattern and analyze the thin sections.

Tests were performed at a rate of 2×10^{-6} mm/s, except for one specimen (bedding inclined at 45° to the loading direction) which was tested at 1.2×10^{-5} mm/s. All core samples were maintained in a chamber at a constant relative humidity (RH) of 70% for at least 2 weeks before testing. This setting allowed samples to stabilize at a realistic semidrained state. The core samples were painted prior to testing with flat black spray paint (Rust-Oleum Painters Touch), then speckled with white spray paint (Figure 1), to perform digital image correlation (DIC) during testing. To calculate the apparent tensile strength (σ_t) from the Brazilian test, the formula provided in *ASTM* [2008] was used:

$$\sigma_t = \frac{2P}{\pi D t} \tag{1}$$

where P is the load (N), D is the sample diameter (mm), and t is the sample thickness (mm). It should be noted that this equation only applies to the case where the tensile fracture originates at the center of the sample and propagates toward the loading platen [e.g., *Perras and Diederichs*, 2014]. In our experiments (section 3.1), however, the fracture appeared to initiate near the loading area, which would invalidate the applicability of the equation (1) to measure the tensile strength. Due to this discrepancy, the tensile strength estimated using the equation (1) is hereinafter referred to as the apparent tensile strength for the purpose of comparison with the experimental results in the literature.

Two samples cored perpendicular to bedding (samples A and B) were loaded with the orientation parallel to the bedding plane, while two samples cored parallel to bedding (samples C and D) were loaded at 45° and

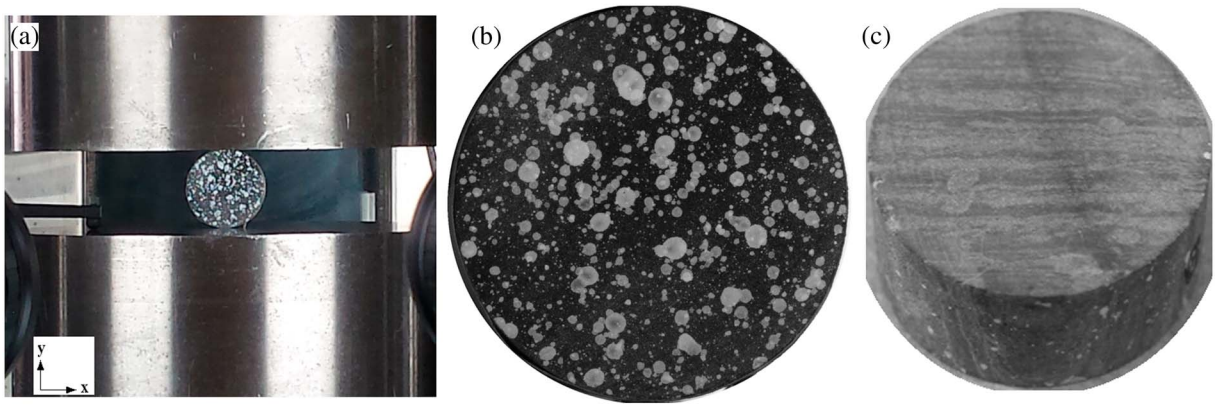

Figure 1. (a) Brazilian test setup for Mancos Shale. Note that a single thickness of masking tape is wrapped to reduce the stress concentration at the loading point. (b) Shale sample painted with black spray and speckled with white spray to perform digital image correlation and (c) unpainted side of the sample.

90° to the bedding plane, respectively. After testing, three thin sections were prepared to analyze the fracture patterns. For samples A and B, the thin sections were taken across the bedding plane instead of along the loading direction because the thin section along the loading direction would show only relatively homogeneous layered features. Here we reported the thin sections only for samples C and D which corresponded to DIC imaging results.

2.3. Digital Image Correlation

Digital image correlation (DIC) is a noncontact optical vision measurement technique. Full field measurements are obtained by applying a unique, nonrepeating pattern to the surface to be measured. A series of images is then captured via digital cameras. By comparing images to a reference image and utilization of subpixel interpolation algorithms, displacement smaller than a pixel can be resolved. The process results in a displacement field of the imaged surface in question (in two or three dimensions depending on the system). From the displacement field, a strain field can be calculated. The interested reader can explore the details of digital image correlation theory and applications in *Sutton et al*. [2000] and *Nguyen et al*. [2011].

In this work, a commercial software program called VIC3D-7®, produced by Correlated Solutions, was utilized to determine the strain field of the shale specimens. Images were captured by a pair of Point Grey Research Grasshopper 5.0 megapixel monochromatic cameras. The cameras were equipped with a pair of Edmund Optics 35 mm machine vision lenses with a 5 mm extension tube. Images were collected with Correlated Solutions VICSnap® software at a rate of 4 frames per second. Subsequently, the image data were processed after completion of the testing with the VIC3D-7® software. The test duration was approximately 4 min, which is in the middle of the target time for the Brazilian test [*ASTM*, 2008]. This procedure resulted in the capture of approximately 1000 images during the test. Although the frame rate was too slow to capture real-time crack growth and propagation, the frame rate employed here was sufficient to provide the evolution of failure in terms of the displacement.

The thinnest possible coat of black paint was applied first to provide a uniform background; then flat white was sputtered over the surface of the core sample. Testing was performed within 1 h of painting to ensure that the paint had the maximum possible ductility to track the specimen without cracking or flaking [*Reu*, 2015]. In general, the strength of the paint and its effect on the mechanical properties of a specimen are negligible. However, *Simpson* [2013] experimentally demonstrated with Mancos Shale that specimens with painted surface influenced the tensile strength, compared to air-dry specimens, which attributed to the change of the internal stress with the painting as suggested by *Knudsen et al*. [2007]. Although the painting may influence the local stress distribution on the surface, samples prepared in the constant RH condition and thin painting layers ($<$500 μm) in this work should minimize the impact of painting on the mechanical properties.

In order to correlate the images with the load-displacement data from the load frame, scaled outputs of load and displacement were collected by VICSnap® each time it took an image. This allows for plotting of processed images coupled with a stress-strain curve shown later in the paper. During processing of the

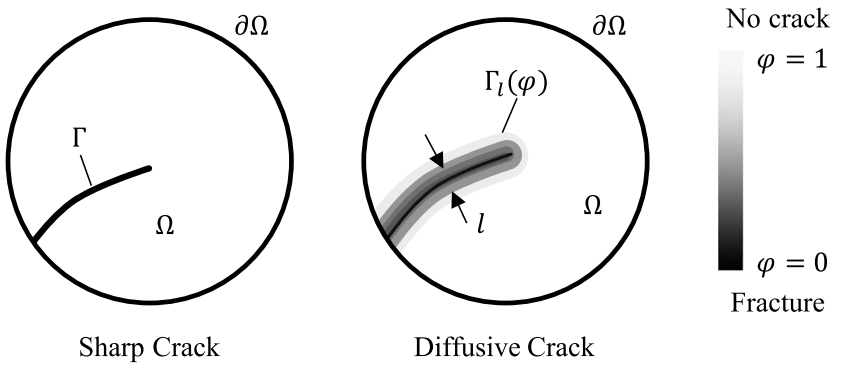

Figure 2. Sharp and diffusive crack topology. Γ indicates the sharp crack surface embedded into the solid Ω, Γ_l (φ) represents the regularized crack surface as a function of the crack phase field (φ), and l stands for the characteristic length scale (reproduced from *Miehe et al.* [2010a]).

DIC data, subsets and step sizes were optimized to minimize noncorrelated points and maximize the resolution of the DIC data (a subset of 61 pixels, with a step size of 9 pixels). Data were processed with an optimized eight-tap interpolation filter with a zero-normalized squared differences criterion, and subsets of data were weighted with a Gaussian function. Image resolution was ~0.02 mm per pixel, and DIC resolution was ~0.2 pixel (4 μm).

2.4. Phase Field Model for Evolving Cracks

In this work, a phase field fracture model based on the generalized Griffith's theory is adopted to simulate the crack initiation and propagation for brittle materials [e.g., *Kuhn and Müller*, 2010; *Borden et al*., 2012; *Hofacker and Miehe*, 2012; *Verhoosel and Borst*, 2013; *Schlüter et al*., 2014; *Heister et al*., 2015]. Since the phase field fracture model employs an implicit function instead of strong discontinuities to represent cracks, it does not require complicated numerical treatments such as generation of enrichment functions [*Dolbow et al*., 2000], dynamic insertion of cohesive elements [*Zhang and Paulino*, 2005], or modification of the mesh [*Mota et al*., 2008]. This approach treats the interfacial zone (i.e., cracks) as a diffusive transition zone represented by a phase field, which takes on values between zero and one, corresponding to fully broken and intact states, respectively. The phase field is incrementally updated by solving governing equations that minimize a free energy functional composed of the bulk strain energy and the fracture energy via the variational principle [*Moelans et al*., 2008].

Figure 2 shows a schematic diagram of a crack represented by the phase field. The phase field is a spatial function that indicates the degree of damage of the material. As such, the crack and intact regions are the locations with the phase field value equal to zero and one, respectively. In the transition zone where the phase field value is $0 < \varphi < 1$, the material is considered partially damaged such that a portion of stiffness and loading capacity persist. In the phase field approach, the characteristic length scale (l) is used to control the diffusive crack. For example, the sharp crack can be represented when l approaches to zero [*Miehe et al*., 2010a]. Neglecting the body force and inertia term, the potential energy functional (Π) that gives the governing equation reads

$$\Pi(\boldsymbol{u},\varphi) = \int_\Omega \frac{1}{2}\left[(1-\kappa)\varphi^2+\kappa\right)\boldsymbol{\sigma}^+(\boldsymbol{u}) : \boldsymbol{\varepsilon}(\boldsymbol{u})]dV + \int_\Omega \frac{1}{2}[\boldsymbol{\sigma}^-(\boldsymbol{u}) : \boldsymbol{\varepsilon}(\boldsymbol{u})]dV + \int_\Omega G_c\left(\frac{1}{2l}\|1-\varphi\|^2 + \frac{l}{2}\|\nabla\varphi\|^2\right)dV - \int_{\partial\Omega}[\boldsymbol{t}\cdot\boldsymbol{u}]dS, \quad (2)$$

and the first variation gives the Euler-Lagrange equations:

$$D_{(\delta\boldsymbol{u})}\Pi(\boldsymbol{u},\varphi) = \int_\Omega \frac{1}{2}\left[(1-\kappa)\varphi^2+\kappa\right)\boldsymbol{\sigma}^+(\boldsymbol{u}) : \boldsymbol{\varepsilon}(\delta\boldsymbol{u})]dV + \int_\Omega \frac{1}{2}[\boldsymbol{\sigma}^-(\boldsymbol{u}) : \boldsymbol{\varepsilon}(\delta\boldsymbol{u})]dV - \int_{\partial\Omega}[\boldsymbol{t}\cdot\boldsymbol{u}]dS, \quad (3)$$

as well as,

$$D_{(\delta\varphi)}\Pi(\boldsymbol{u},\varphi) = \int_\Omega[((1-\kappa)\varphi)\boldsymbol{\sigma}^+(\boldsymbol{u}) : \boldsymbol{\varepsilon}(\boldsymbol{u})]\ \delta\ \varphi dV - \int_\Omega G_c\left(\frac{1}{l}(1-\varphi)\delta\varphi\right)dV + \int_\Omega G_c(l\nabla\varphi\cdot\nabla(\delta\varphi))dV, \quad (4)$$

where $\boldsymbol{u}$ is the displacement, φ is the phase field variable, κ is a positive regularization parameter for the elastic energy with $\kappa \ll 1$ [*Miehe et al*., 2010a; *Borden et al*., 2012; *Heister et al*., 2015], $\boldsymbol{\sigma}$ is the stress tensor which is decomposed into tensile ($\boldsymbol{\sigma}^{+}$) and compression ($\boldsymbol{\sigma}^{-}$) parts for correct modeling of shear forces under compression following *Miehe et al*. [2010b], ε is the infinitesimal strain tensor defined as $\varepsilon = 1/2(\nabla \boldsymbol{u} + \nabla^{\mathrm{T}} \boldsymbol{u})$, G_c stands for the critical energy release rate that is related to fracture toughness [e.g., *Anderson*, 2005; *Jaeger et al*., 2009; *Chandler et al*., 2016], and $\boldsymbol{t}$ indicates the traction force on the boundary. The hydro-mechanical coupling effect is not considered in this study. Hence, the finite element model only updates displacements of solid and crack phase field at each incremental step.

In equation (2), the first two terms are the elastic strain energy corresponding to tension and compression modes, respectively. The sum of two terms gives the total elastic strain energy over the domain (i.e., the bulk energy E_B). The third term represents the crack surface energy (i.e., E_C) that is approximated by the volume integration of diffusive crack phase field. The last term is the work done by the external traction. The bulk energy indicates the macroscopic strain energy over the model domain of which the peak value is related to the effective crack toughness [cf. *Hossain et al*., 2014]. E_B dissipates as crack initiates and propagates. E_C identifies the onset and behavior of cracks, which compensates the dissipation of bulk energy. In this work, we compare the calculated bulk and crack energies (E_B and E_C) to analyze the crack initiation and coalescence under various configurations of the model domain (section 3.2). Furthermore, a predictor-corrector scheme for local mesh adaptivity-mesh refinement around the cracks is used to improve the accuracy and computational cost [*Heister et al*., 2015].

The implementation of the numerical model leverages the open source finite element library, deal.II [*Bangerth et al*., 2007, 2013] interfaced with p4est mesh handling library [*Burstedde et al*., 2011], and Trilinos project—a growing collection of mathematical software libraries for solving a large-scale, complex multiphysics engineering and scientific problems [*Heroux and Willenbring*, 2012; *Salinger et al*., 2013]. Recently, deal.II has been adopted as a finite element library for geomechanics applications to resolve solid deformation and fluid diffusion coupling problems [*White and Borja*, 2008, 2011] as well as different poromechanics problems including pressurized fracture propagation [e.g., *Heister et al*., 2015; *Choo and Borja*, 2015; *Choo et al*., 2016; *Na and Sun*, 2017]. In this study, we slightly modify the phase field model published in *Heister et al*. [2015] by introducing the spatial heterogeneity and anisotropy. Note that the theory, implementation, and verification of the phase field model are not the focus of this paper. Interested readers can refer to a vast amount of literature on the phase field method [e.g., *Miehe et al*., 2010a; *Kuhn and Müller*, 2010; *Borden et al*., 2012; *Verhoosel and Borst*, 2013; *Hofacker and Miehe*, 2013; *Heister et al*., 2015]. The detailed numerical scheme and monolithic formulation of Euler-Lagrange PDE system to resolve elasticity and phase field can be found from *Heister et al*. [2015]. In addition, the detailed description of the mesh adaptivity is provided and the code base is shared through an open-source repository (https://github.com/tjhei/cracks).

For numerical simulations of the Brazilian test in this work a number of assumptions are employed as followings:

1. Within each layer, the elastic response is isotropic (except Cases 6 and 7).
2. Within each layer, the material is homogeneous.
3. The materials for each constituent are in the purely brittle regime, and hence, ductility is not considered.
4. The small-scale yielding condition is valid.
5. The loading of the Brazilian test is idealized as a prescribed displacement over a fixed contact area.
6. The contact area between the specimen and the test device is frictionless.

As a result, the modeling setup does not reflect the valid Brazilian test conditions in heterogeneous materials. Nonetheless, with proper interpretation of simulation results the phase field modeling employed in this work can provide insightful results for parametric studies.

2.5. Numerical Simulations

A comprehensive series of numerical simulations has been performed to analyze how spatial heterogeneity and anisotropy of elasticity affect the effective toughness and crack propagation of materials under the Brazilian test conditions. A two-dimensional circular domain with a diameter of 26.0 mm is used with a linear elastic model as shown in Figure 3. The displacement boundary condition is applied at the top and bottom parts of the numerical domain, and the contact area (or the arc length S in 2-D) has 5° of the central angle (θ)

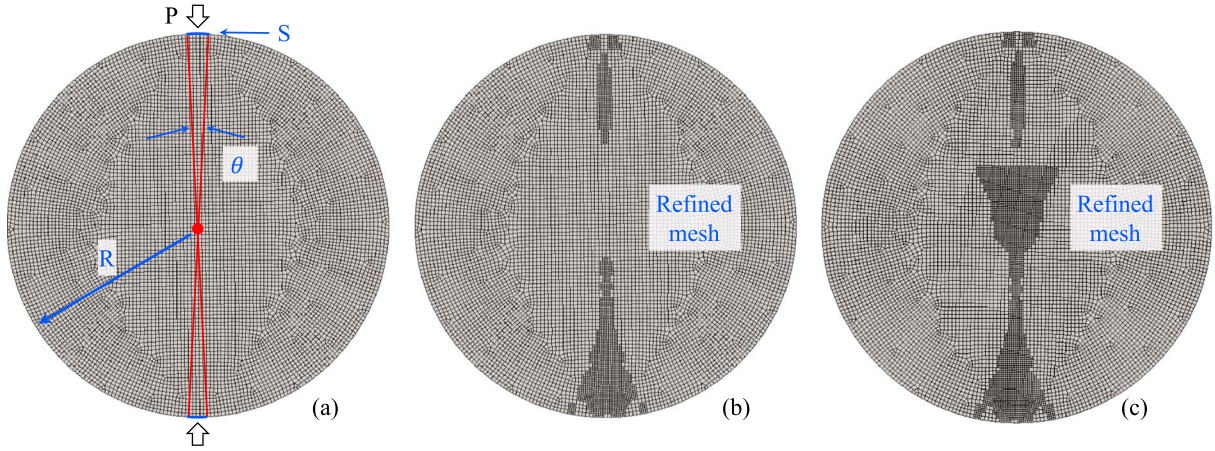

Figure 3. Numerical setup for the Brazilian test. (a) The initial mesh (8880 elements), the radius (R = 13 mm), and the central angle (θ = 5°) by the arc length (S) over which the boundary condition P is distributed radially. (b and c) The progressive mesh refinement with crack propagation. The meshes in Figures 3b and 3c correspond to Figures 6a2 and 6a3, respectively.

to replicate the experimental setup. The vertical displacements of the contact area between the loading frame and the specimen are prescribed incrementally to compress the specimen (Figure 3).

As mentioned previously in section 2.4, we assume that the contact between the loading frame and the specimen is frictionless and is always remained the same. This is a simplification of the real experiment in which the contact area may change and sliding may occur. Furthermore, the assumption that the contact is always intact also makes the simulations easier to exhibit sharp displacement gradient at the edge of the loading area. This concentration of strain may in return lead to higher strain energy density near the edge of the loading area. Hence, the onset of crack may be more likely to initiate near the edge of the disc in numerical simulations. This limitation can be presumably overcome by using frictional contact models. Such an improvement is outside the scope of the current study. It is also noted that the contact area between the specimen and the loading platen has a significant influence on the Brazilian test and its validity [*Fairhurst*, 1964; *Li and Wong*, 2013; *Perras and Diederichs*, 2014]. A small contact area may cause the stress concentration around the loading platen, which may lead the crack to initiate at a point away from the center of the specimen [cf. *Andreev*, 1991a].

The phase field model requires sufficiently fine meshes relative to the length-scale parameter to achieve numerical convergence. In this work, the adaptive mesh refinement algorithm in *Heister et al*. [2015] is used. In each incremental loading step, the trial displacement and phase field are first sought by solving the equations (3) and (4). If the phase field value of any finite element reaches the threshold (=0.3 in this work), then the finite element is refined (Figure 3). If any mesh refinement is triggered, the solver must be rerun to reach the new equilibrium (equations (3) and (4)) for the modified mesh. This process is repeated until there is no need for further refinement. In this study, each finite element may at most be refined once during the simulation. It should be noted that the refinement of the mesh may occur multiple times during numerical simulation. The following section describes the different numerical domains and the parameters tested for various simulation scenarios.

2.6. Numerical Scenarios

2.6.1. Homogeneous Domain

A number of simulations are performed in a homogeneous domain, which is composed of linear elastic, isotropic material. The cases in the homogeneous domain serve as the verification benchmarks of model implementation. First, the stress distribution calculated from the homogeneous domain is compared against the analytical solution [*Hondros*, 1959]. Then, we evaluate the sensitivity of material parameters. The reference values of the main parameters are provided in Table 1. Among four examined parameters, the linear elastic response is characterized by Young's modulus (E) and Poisson's ratio (ν). It is assumed that the surface area created by fracturing requires a supply of energy equal to or greater than the critical energy release rate (G_c) based on Griffith's theory [*Anderson*, 2005]. As described in section 2.4, the characteristic length (l)

Table 1. Reference Input Parameters of Homogeneous Numerical Model for Material Sensitivity Test

Parameter	Description	Value	Unit
E	Young's modulus	20.0	GPa
ν	Poisson's ratio	0.20	–
G_c	Critical energy release rate	0.01	N/mm
l	Characteristic length	0.20	mm

inserted in the phase field model is used to regularize the governing equations. Note that l can be qualitatively interpreted as a means to control the thickness of the damage localization zones and affect the critical stress at which crack nucleation occurs [*Miehe et al*., 2010b; *Borden et al*., 2012].

We perform multiple simulations with Young's modulus (E) varying from 10.0 to 80.0 GPa and Poisson's ratio (ν) from 0.1 to 0.3 to assess the effect of these key material parameters on the global constitutive responses (see Appendix A). This sensitivity analysis is intended to identify the influence of elastic properties on the behavior of an ideal isotropic material under the Brazilian test condition. These values are chosen based on the representative shale materials with various compositions in the literature [e.g., *Sone and Zoback*, 2013a, 2013b]. In addition, simulations with different critical energy release rates are conducted (G_c ranging from 0.01 to 0.10 N/mm based on the measurement in *Chandler et al*. [2016]), and the effect of characteristic length (l) are tested as well.

2.6.2. Layered Domain With Isotropic Properties (Cases 1–5)

The layered system with two isotropic stiff and soft materials is used to evaluate the impact of elastic material properties and the orientation of multiple layers on crack propagation and macroscopic effective fracture toughness. The simulation scenarios are presented in Table 2. Three different cases (Cases 1–3) in the layered domain are employed to account for different volume fractions of the stiff and soft layers. For all three cases the effect of layer orientation on crack patterns is evaluated under three different bedding orientations (90°, 45°, and 0°) with respect to the loading direction, which follows the experimental setup. Note that the volume fraction of Case 1 approximately represents the average of stiff and soft volumes in Mancos Shale used in the experiment.

Shale is composed of layers of intrinsically anisotropic materials. Hence, a more comprehensive modeling effort may require the identifications of principal directions and the corresponding elastic moduli of each layer [*Backus*, 1962]. For simplicity, we follow the isotropy assumption used in *Sone and Zoback* [2013a, 2013b] and assume that shale consists of two constituents (i.e., stiff and soft layers) with elastically isotropic property in a simplified layered domain (only Young's modulus is different for stiff and soft components). This simplification is partially justified by the observations on shale composed of relatively weak (e.g., clay and organics) and strong (e.g., quartz, calcite, and feldspar) materials as in *Sone and Zoback* [2013a, 2013b]. Nevertheless, as shown in the numerical examples, the isotropy assumption may also lead to a nonnegligible discrepancy.

Table 2. Descriptions for Different Numerical Scenarios (Seven Cases)[a]

Numerical Scenarios	Volume Fraction		Effective Elastic Modulus	
	Stiff Layer	Soft Layer	Reuss (E_l)	Voigt (E_u)
Case 1	62.6%	37.4%	13.21 GPa	45.91 GPa
Case 2	75.0%	25.0%	18.06 GPa	53.90 GPa
Case 3	40.5%	59.5%	8.62 GPa	31.56 GPa
Case 4	Reduced layer thickness from Case 1 with the volume fraction			
Case 5	Inclusions of defects into stiff layers from Case 4			
Case 6	Homogenization of the layered system based on Case 1			
Case 7	Layered system with anisotropy in soft layer based on Cases 1 and 4			

[a]For Cases 1 to 5, both stiff and soft layers are assumed to be isotropic with Young's moduli of 70.0 GPa and 5.6 GPa, respectively (same Poisson's ratio 0.20); Reuss and Voigt bounds are based on the assumptions of uniform stress and strain in the composite, respectively [*Lama and Vutukuri*, 1978]. For Case 6, the transversely isotropic effective medium is obtained via homogenization based on the layered system with two constituents (see section 2.6.3); for Case 7, the layered system with isotropic stiff and transversely isotropic soft layers are used (Table 3). For all cases, the fixed numerical values of G_c and l are used (Table 1).

For Mancos Shale samples used in the experiment of this study, major components of the stiff layer are quartz and calcite, and the rest are predominantly clay minerals with low total organic content (<1.0 wt %) [*Grigg*, 2016]. Based on the literature [e.g., *Sone and Zoback*, 2013a, 2013b], the elastic moduli of stiff and soft layers are set to 70.0 and 5.6 GPa, respectively. The Poisson's ratio of both layers is assumed to be 0.2 [e.g., *Kumar et al*., 2012a, 2012b; *Gercek*, 2007]. The critical energy release rate and characteristic length in the phase field reported in Table 1 are used for both layers. The effective lower (E_l—Reuss bound) and upper (E_u—Voigt bound) bounds of two-constituent system are also estimated based on the volume fraction of the two constituents [e.g., *Lama and Vutukuri*, 1978].

We perform additional numerical simulations to account for spatial elastic heterogeneity in a simple way. First, Case 4 increases the number of layers by reducing the thickness of each layer, but the volume fraction of stiff and soft layers is consistent with Case 1 (Table 2). In Case 5 the simple defect patterns on the stiff layers are introduced, while the layer thickness condition is the same as in Case 4 (Figure 14).

In the layered model, the vertical thickness of laminated layers ranges from 1.0 mm to 4.5 mm in the diameter of 26 mm based on the petrographical analysis of Mancos Shale samples [*Grigg*, 2016]. The thin laminations often exhibit parallel layering or bedding at the submillimeter to centimeter scales, and irregular and complex layerings are observed at submillimeter scale due to various depositional environments and diagenesis [*Blatt et al*., 2006; *Grigg*, 2016]. Complex microstructural attributes may occur due to the overprinting of cementation and diagenesis during the burial of the sediments and postburial structural deformation (i.e., fracturing) of the rocks.

2.6.3. Homogenization and the Layered System With Anisotropy in Soft Layer (Cases 6–7)

A multiscale-based understanding of heterogeneous geomaterials such as shale formations is fundamental to quantifying the scale dependence of mechanical behaviors in geomaterials. However, applying our basic findings to the real world has been hampered by a lack of understanding of the connection between microscopic parameters and macroscopic properties. For Case 6, we obtain the homogenized transversely isotropic effective medium and investigate the simulated fracture patterns compared to the specimen with the layered system composed of two isotropic materials (Table 2). The transversely isotropic model properties are determined based on the layered isotropic materials' properties in Case 1. By assuming that the effective medium exhibits the same G_c and l as reported in Table 1, we employ the equation (5) to obtain the 2-D plane strain elasticity tensor of the effective medium based on the layer-averaging method introduced in [*Berryman*, 1998] [cf. *Backus*, 1962].

$$\begin{bmatrix} \sigma_{11} \\ \sigma_{22} \\ \sigma_{12} \end{bmatrix} = \begin{bmatrix} a & f & 0 \\ f & c & 0 \\ 0 & 0 & 2d \end{bmatrix} \begin{bmatrix} \varepsilon_{11} \\ \varepsilon_{22} \\ \varepsilon_{12} \end{bmatrix}, \tag{5}$$

$$\text{where } a = \left\langle \frac{\lambda}{\lambda + 2\mu} \right\rangle^2 \left\langle \frac{1}{\lambda + 2\mu} \right\rangle^{-1} + \left\langle \frac{\mu(\lambda + \mu)}{\lambda + 2\mu} \right\rangle, \tag{6}$$

$$c = \left\langle \frac{1}{\lambda + 2\mu} \right\rangle^{-1}, \tag{7}$$

$$f = \left\langle \frac{\lambda}{\lambda + 2\mu} \right\rangle^2 \left\langle \frac{1}{\lambda + 2\mu} \right\rangle^{-1}, \tag{8}$$

$$\text{and } d = \left\langle \frac{1}{\lambda} \right\rangle^{-1}. \tag{9}$$

Here the stress, strain, and elasticity tensors are presented using the Voigt convention for the transversely isotropic material description whose symmetry axis is in x_2 direction (y axis or vertical direction) [*Berryman*, 1998]. Parameters of a, c, f, and d are obtained using the Lamé constants λ and μ, while $\langle\cdot\rangle$ stands for weighted average using the volume fraction of two layers [*Berryman*, 1998]. Note again that we adopt the volume fraction of stiff (62.6%) and soft (37.4%) layers from Case 1 for homogenization. The homogenized properties may not be consistent with the elastic anisotropy of the real shale. This study, however, may provide an

Table 3. Material Properties for Stiff (Isotropic) and Soft (Transverse Isotropic) Layers[a]

–	Stiff Layer	Soft Layer
Properties	E = 70.0 GPa ν = 0.2	E_1 = 5.6 GPa, ν_{12} = 0.3 E_3 = 2.8 GPa, ν_{13} = 0.15 G_{13} = 1.7 GPa

[a]Notation: the rotational axis of symmetry is parallel to the x_3 axis, and x_1-x_2 coordinate system planes are identical [cf. *Ong et al*., 2016].

understanding of microscopic (homogenized domain) and macroscopic (explicitly layered domain) information in numerical consideration. The elasticity tensor for different layer orientations is generated using the transformation matrix in 2-D [cf. *Li et al*., 2015].

Finally, we assign a transversely isotropic model to the soft layer instead of the isotropic soft material (Case 7). As in the two-constituent composite models (Cases 1 and 4), we preserve the isotropic model for the stiff layer. This scenario is to consider the anisotropy of soft constituent based on its components. The elastic properties of shale are known to be strongly anisotropic, and the amount of clay and organic content, as well as the shale fabric, is closely related to the degree of anisotropy [e.g., *Sone and Zoback*, 2013a]. Furthermore, the platy clay minerals as the soft component often exhibit a preferred orientation. By adopting the transversely isotropic model for the soft layer, we evaluate the influence of anisotropy in the soft layer on the crack propagation and effective toughness of the two-composite model.

In Case 7, the previous isotropic material parameters for stiff layers are used (Table 3); Young's modulus = 70.0 GPa and Poisson's ratio = 0.2. For the soft layers, the transverse isotropic model is adopted, in which the plane of isotropy is assumed to be aligned with the bedding (or the orientation of layers). The material properties are determined based on the fact that intact transverse isotropic rocks are typically stiffer in the plane of isotropy than in the direction of symmetric axis [*Jaeger et al*., 2009]. We presume that the rotational axis of symmetry is parallel to the x_3 axis, and x_1-x_2 coordinate system planes are bedding planes. We then set the material parameters as Young's modulus (E_1 = 5.6 GPa) and Poisson's ratio (ν_{12} = 0.3) in the plane of isotropy (i.e., along the bedding) and E_3 = 2.8 GPa and ν_{13} = 0.15 in the normal to the isotropic plane (i.e., perpendicular to the bedding). We adopt E_1 from the isotropic model for soft layers used in Case 1. G_{13} denoted by the shear modulus along the perpendicular direction of the isotropic plane is assumed to 1.7 GPa [cf. *Amadei*, 1996; *Debasis and Kumar*, 2016; *Ong et al*., 2016]. The material parameters for stiff (isotropic) and soft (transverse isotropic) layers are summarized in Table 3.

The numerical results are subsequently analyzed including crack initiation, propagation, and fracture pattern. Besides, macroscopic parameters such as the macroscopic bulk and crack energies (E_B and E_C) are computed to compare the effective fracture toughness. It should be noted that microstructural and compositional heterogeneity at micron and submicron scales will influence the crack initiation and propagations significantly, which is not considered in this work. Instead, our numerical model of the layered system is extremely simplified to idealize the strongly layered bedding configuration with two constituents. A further study is required to quantify the effect of the microheterogeneity.

3. Results and Discussion

3.1. Experimental Results

The axial stress and vertical displacement for all four samples are shown in Figure 4. The distributions of horizontal tensile strain (ε_{xx}) for samples A–D computed from DIC of the Brazilian disk with the thin-section images of samples C and D after the testing are shown in Figure 5. As described earlier, the loading and displacement were applied simultaneously with image acquisition, and the corresponding strength points of each strain distribution are also presented. For all testings the apparent tensile strengths (σ_t) computed using equation (1) are obtained: σ_t (4.55 MPa) at 90° was higher than 2.57 MPa at 45° and lower than 4.72–6.50 MPa at 0° (bedding parallel to the loading direction). Although these results do not provide a conclusive result of the impact of bedding angle on the apparent tensile strength due to a small number of samples, our σ_t values at 0° (4.72–6.50 MPa) are within the range of 5.8 ± 0.6 MPa [*Chandler et al*., 2016] and 6.4 ± 2.3 MPa [*Kennedy*, 2011]. It should be noted that *ASTM* [2008] standard is based on the assumption that the crack initiates at the

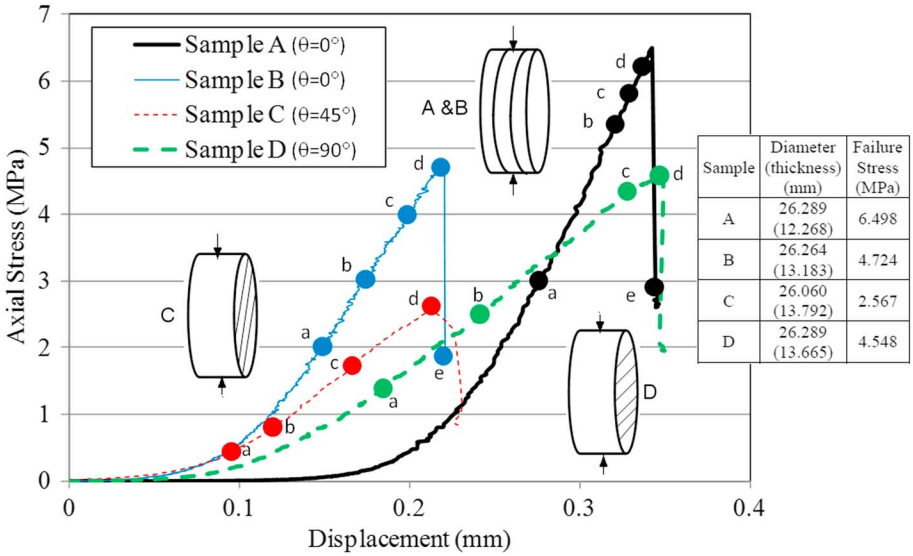

Sample	Diameter (thickness) (mm)	Failure Stress (MPa)
A	26.289 (12.268)	6.498
B	26.264 (13.183)	4.724
C	26.060 (13.792)	2.567
D	26.289 (13.665)	4.548

Figure 4. Experimental results. Axial stress and vertical displacement obtained from the Brazilian tests. Schematics illustrate the loading angle with respect to the bedding orientation of samples.

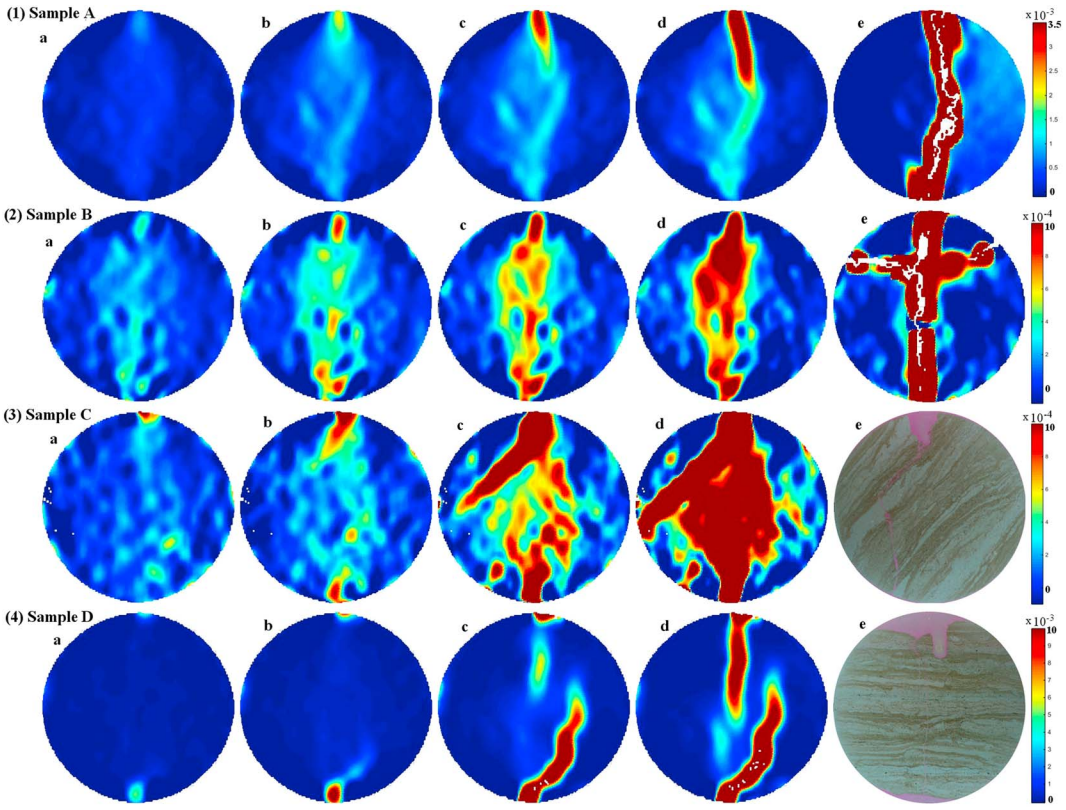

Figure 5. The distribution of horizontal strain (ε_{xx}—positive in tension) computed from DIC with the thin-section image of the Brazilian disk after testing for samples C and D. The pink colored epoxy in thin section (e) indicates the severely broken part (see high resolution images of thin section and crack propagation at the end of testing on the painted sample in Figures S1 and S2).

center of the specimen. Although DIC was not fast enough to capture the exact locations of actual crack initiation, the change of strain distribution over time indicates that the cracks apparently did not initiate at the center of the specimen in our experiments. As a result, the apparent tensile strength estimated using equation (1) should be interpreted with caution. Furthermore, σ_t across the bedding plane (90°) was higher than at 0° in the Brazilian test of multiple Mancos Shale specimens [e.g., *Simpson*, 2013; *Mokhtari*, 2015; *Chandler et al*., 2016]. The different tendency is likely due to the compositional heterogeneity of samples used in this work as well as sample preparation. In particular, *Chandler et al*. [2016] reported that σ_t values at 90° (the bedding perpendicular to the loading direction) had much higher scattering than other directions, which was attributed to the anisotropic material strength causing the fracture to deflect into the weaker bedding plane direction.

As shown in Figure 5 (sample D), the thin-section image illustrates the deflection of fracture near the top loading contact area, which may account for the lower σ_t across the bedding plane (90°). Another contributing factor is the discrepancy on the compositional heterogeneity. Petrographical analysis of the thin-section based on a slight modification of textural classification of mudstones from *Folk* [1980] and *Lazar et al*. [2015] shows that sample A is predominantly cored in the sandy coarse mudstone consisting of more than two-thirds course/medium mud (62.5 to 8 μm) and 10 to 50% sand grains (2000 to 62.5 μm). Meanwhile, sample B is cored in the sandy coarse mudstone and medium mudstone (less than 10% sand grains and between one third and two thirds of coarse/medium mud with fine mud grains ($<$8 μm) for the rest), whereas sample C in the medium mudstone, and sample D in the medium mudstone and sandy medium mudstone [*Grigg*, 2016]. Based on the macrolithofacies description, samples A and B are stronger than the others with sample C as the weakest. Hence, σ_t values measured in this work were also significantly influenced by composition rather than the bedding angle with similar lamination structure. This result will be further analyzed in numerical simulation results.

The tensile strain distribution based on the DIC reveals the fracture patterns (i.e., crack initiation and propagation) over the course of the Brazilian test (Figure 5). First, samples A and B were loaded with bedding parallel to the loading direction; hence, these cases can be considered to be a sum of multiple homogeneous layers along the loading direction. For 2-D case, the *Hondros*' [1959] solution indicates that the tensile stress in the middle part along the loading direction is relatively constant and the compressive stress increases from the center to both loading points. As a result, cracks initiate from the center when the tensile stress overcomes the tensile strength. However, *Yu et al*. [2006] revealed that the tensile stress distribution on the surface of a 3-D disk is different from that in the middle of the disk. More recently, *Li and Wong* [2013] numerically demonstrate that the maximum tensile stress and strain are located at ~10% of the disk diameter away from the loading points on the 3-D surface, while the maximum tensile stress is located in the middle and the maximum tensile strain is located near the loading points. Figure 5 reveals that the tensile strain for samples A and B occurred near the loading points at first, propagated into the central portion, and coalesced along the loading direction. In addition, the DIC results reveal that the tensile strain was locally concentrated in the central region along the loading direction. These local concentrations of the tensile strain are likely due to heterogeneous material properties (e.g., high clay regions) and possibly existing flaws and cracks.

For sample C oriented at 45°, the tensile strain first accumulated near the contact area, then the crack started to propagate along the clay-rich microlithofacies (e.g., brownish color in a thin section) adjacent to the stiff sandy microlithofacies (e.g., bright color in a thin section) as shown in Figure 5 at the third row. This fracturing along weakness planes has been described as layer activation [*Tavallali and Vervoort*, 2010b] or Mode II fracture [*Mighani et al*., 2016]. As a result, the tensile strain field was much larger at 45° than at 0°. The thin section clearly shows the sliding along the clay-rich layers (in dark pink) and high damage zone (in very light pink). A vertical crack propagated through the weak materials on the left from the loading plane, which coalesced into the sliding crack. As a result, the apparent tensile strength was lower than other cases. For sample D at 90°, the tensile strain occurred near the loading points at first. However, two distinct cracks were initiated and propagated in the middle along the loading direction, while the tensile strain also grew at an inclined angle from the bottom. Eventually, all cracks coalesced in the middle. Due to crack growth from both ends, there are two main cracks in the upper region of the thin section.

The thin section (Figure 5e for samples C and D and Figures S1–S2 in the supporting information for high-resolution images) shows that the anisotropic heterogeneity with the inclined layers and varying thickness strongly affects the nature and patterns of crack initiation and propagation. In sample C, for example, the

crack initiation starts from the top loading point and follows along the inclined layers due to their orientations. Starting from the bottom part, another crack propagates through the center of the domain and develops the main crack. We note that the pink epoxy of the thin section indicates the severely broken state around the top loading platen. The heterogeneity of the specimens is due to sedimentation and diagenesis processes as evidenced by the presence of bioturbation, possible ripple marks, and soft sediment deformation [*Grigg*, 2016]. In addition to the experimental results of this study, the tendency of fracture patterns due to anisotropic feature (e.g., layered system) can also be found from the reference [e.g., *Simpson*, 2013; *Mighani et al*., 2014; *Wang et al*., 2016; *Mighani et al*., 2016]. The impact of flaws as well as layer orientations on the direction of crack propagation will be investigated in the numerical simulation.

3.2. Simulation Results and Discussion

3.2.1. Homogeneous Domain

All simulation results in the homogeneous domain are provided in Appendix A. The comparison of tensile and compressive stress distributions between numerical and analytical results is shown along the vertical central line (i.e., the loading direction) in Figure A1. The simulated elastic responses show good agreement with the analytical solutions by *Hondros* [1959]. As discussed previously, the small contact area in this simulation ($\theta = 5.0°$) leads to stress concentration near the loading contact areas [cf., *Fairhurst*, 1964; *Andreev*, 1991a]. The loading condition results in crack initiation near the loading platen instead of in the center of the disk specimen. The effect of the contact area between the loading platen and the specimen on the crack initiation and propagation is shown in Figure A2. Recall how the contact area is related to the loading angle (θ) in Figure 3. This study demonstrates that the crack initiates near the loading area when $\theta = 5.0°$. Our preliminary results of the boundary condition with $\theta = 5.0°$ tend to match the experimental observation better than with $\theta = 17.5°$ in the layered domain. Hence, we decided to use $\theta = 5.0°$ for the rest of simulations in this work. Interested readers can refer to recent review works [*Li and Wong*, 2013; *Perras and Diederichs*, 2014] on the location of crack initiation during the Brazilian test and the effects of the boundary loading condition.

The stress-axial displacement relationships for four model parameters (Table 1) are shown in Figure A3. The range of each parameter for sensitivity analysis is provided in Table A1. In summary, Young's modulus significantly affects the stress-axial displacement relationship as expected, while Poisson's ratio (0.1 to 0.3) shows minor impact. The critical energy release rate (G_c) is highly related to the strength of the material. Since G_c represents the crack resistance or fracture toughness, a lower G_c value results in fast failure at a lower stress. The characteristic length scale (l) affects the mechanical strength under the Brazilian test as discussed in *Miehe et al*. [2010b] and *Borden et al*. [2012].

3.2.2. Case 1: Influence of Layer Orientations on Crack Propagation

The fracture patterns obtained from the specimens of different layer orientations (90°, 45°, and 0° with respect to the vertical loading direction) are shown in Figure 6. For visualization purposes, the phase field values of 0.0 to 0.3 were chosen. Crack propagations are depicted over the layers (stiff layer with blue; soft layer with gray). The phase field zero represents the fully cracked region (the color red in the figure). For the horizontal layers Figures 6(A1) to 6(A4), the cracks initiate from the top and bottom parts where the loading contacts are located. The crack, starting at the lower central region in Figure 6(A1), propagates both upward and downward and eventually develops into the main fracture combined with other cracks. For the inclined layers (Figure 6(B1) to 6(B4)), the main crack initiates from the top and propagates along the soft layer. Another crack initiated from the bottom moves upward, which can be compared to the experimental observation (Sample C in Figure 5). For the vertical layer (Figures 6(C1) to 6(C4)), the main crack develops vertically in the stiff layer, and additional crack openings are created along the interface of the two layers. These cracks, combined with the existing cracks, build the main crack following the vertical line. Overall, the simulation results in Case 1 indicate that the distribution of elastic layers against the loading direction significantly influences fracture patterns.

Figure 7 shows the stress distributions using horizontal and shear components obtained from each numerical element. Note that since the global coordinates are horizontal (x) and vertical (y) axes [e.g., *Erarslan and Williams*, 2012; *Li and Wong*, 2013; *Dan and Konietzky*, 2014; *Tan et al*., 2015], the maximum tensile stress is not exactly aligned to the horizontal direction. The phase field values of 0.0 to 0.1 are used to reflect the damaged zone (white spaces) that includes both crack and severely broken parts. For the horizontal layer (Figures 7(A1) to 7(A2)), the horizontal stress in tension is concentrated around the crack tips within the stiff layer (i.e., local stress concentration) before the crack propagates. More stress concentration tends to occur at the interface of the two layers, where the layers are inclined (Figures 7(B1) to 7(B2)) or vertically aligned

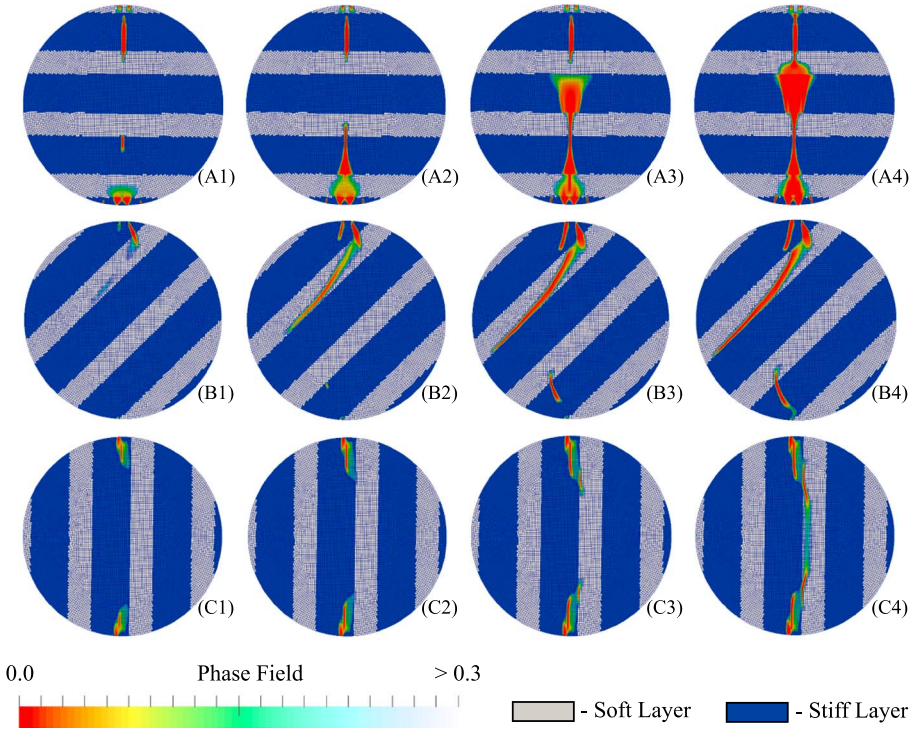

Figure 6. Sequence of crack propagation in Case 1 (stiff: 62.6%; soft: 37.4%) for each orientation of layers: (a) horizontal layer, (b) inclined layer, and (c) vertical layer. The range of phase field from 0.0 to 0.3 is selected for visualization purpose to highlight fracture over the layered domain. Young's moduli of stiff and soft layers are 70.0 and 5.6 GPa, respectively.

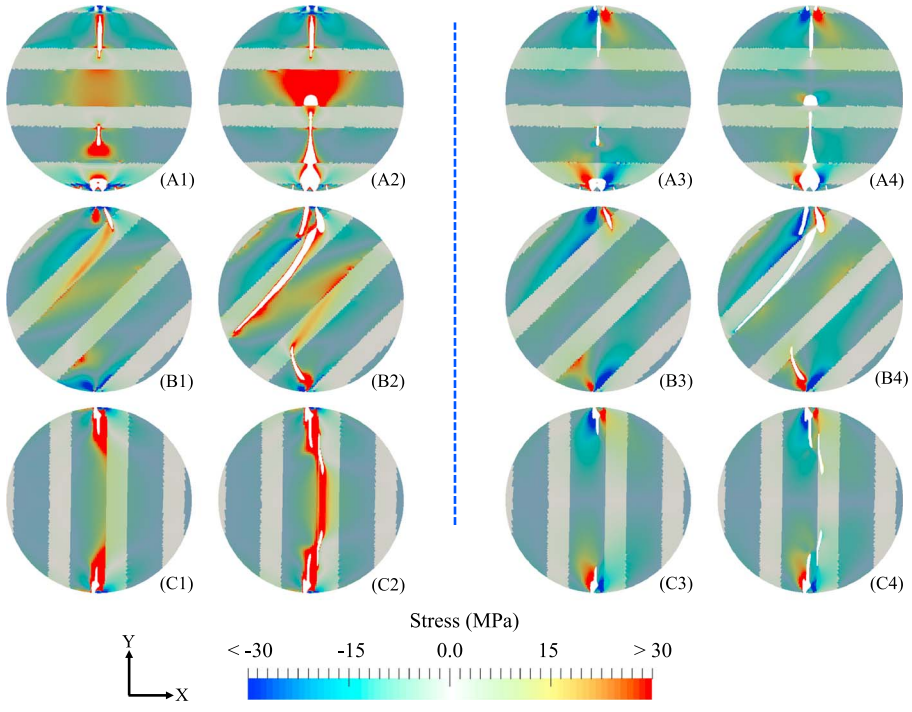

Figure 7. Stress distribution in the specimens composed of layers of different orientations in Case 1 (stiff: 62.6%; soft: 37.4%). The left and right two figures indicate the normal stress along *x* direction and the shear stress distribution, respectively. The stress ranges from 30 MPa to −30 MPa for visualization purpose. The damaged zone is represented using the phase field values of 0 to 0.1 to indicate cracked region (white spaces), which includes both crack and severely broken part due to material heterogeneity as seen in the experimental thin section (Figure 5).

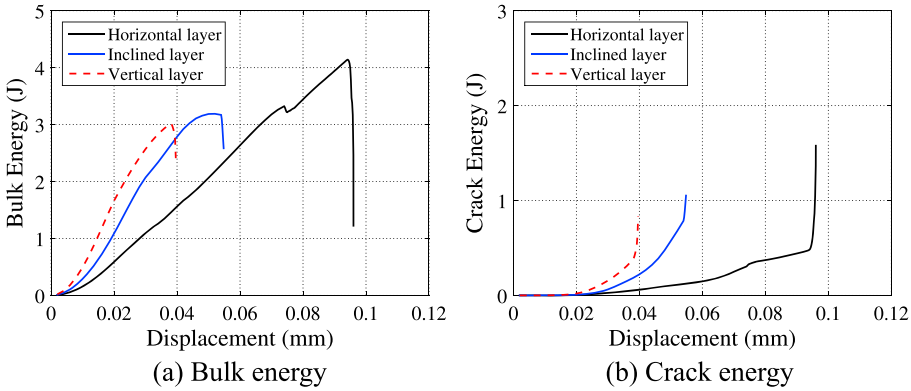

Figure 8. Comparison of (a) bulk and (b) crack energies for different orientation of layers in Case 1 (stiff: 62.6%; soft: 37.4%). The relevant crack patterns and stress distributions can be found in Figures 6 and 7.

(Figures 7(C1) and 7(C2)) layers. While the predominant mode appears to be a tensile fracture, the shear stress concentration is mostly observed around the loading points with partial cracks. As a result, the shear component shows a limited effect on crack growing processes [e.g., *Hobbs*, 1964; *Li and Wong*, 2013].

Finally, bulk and crack energies (E_B and E_C; see section 2.4) are used to investigate effective fracture toughness in the layered system (Figure 8). First, the highest bulk energy is required for the horizontal layer with the orientation of 90°. As shown in Figure 8, the horizontal layer (90°) demands more displacement to reach the maximum bulk energy compared to the inclined (45°) and vertical (0°) layer conditions. These results indicate how the orientation of layers influences the effective fracture toughness. The role of the soft component in the horizontal bedding condition is barely observable since the main crack propagates through both stiff and soft layers (Figure 6). In the inclined and vertical bedding orientations, however, the soft layers play a significant role as the preferred pathway for crack growth. The crack energy profile in Figure 8 further indicates that more displacement occurs for the horizontal layer case during the early stage of loading, compared to the other layer orientations. This is evident in Figure 6 that multiple cracks are developed for the horizontal layer case, whereas the major cracks are developed with the small displacement for the inclined and vertical layer orientations.

3.2.3. Cases 2 and 3: Influence of Volume Fraction of Layers on Crack Energy

The different volume fractions of stiff and soft constituents (Cases 2 and 3) were adopted to evaluate how the composition variations of the layered system influence the crack patterns and the effective fracture toughness (Figures 9–11). Table 2 presents the effective Young's moduli of Cases 1–3 for comparison. The overall crack propagation patterns for the horizontal and inclined layers in Case 2 (higher fraction of the soft layer) have similar patterns to those in Case 1 (Figures 9(A1) to 9(A4) and 6(A1) to 6(A4)). As the layer thickness changes, the locally damaged patterns in the bottom soft layers are slightly different, but the impact on the fracture behavior appears to be minor. Along the inclined layers, the main crack in Case 2 propagates within the soft layer just as it does in Case 1. For the vertical layer (Figures 9(C1) to 9(C4)) in Case 2, the independent crack is initiated in the soft layer in addition to two other cracks propagated from the loading points. One possible reason, besides the change of layer thickness, could be due to the asymmetric distribution of the two layers, which may have a significant impact on the stress distributions. The similar fracture behavior in Cases 1 and 2 is further identified from the bulk energies in Figure 11.

The specimens composed of horizontal and vertical layers in Case 3 (higher fraction of the soft layer) exhibit similar crack patterns to those in Case 1. However, for the inclined layer in Case 3 (Figures 10(B1) to 10(B4)), the multiple crack branches coalesce and form the main crack that propagates through the central region. Conversely, the main crack is contained within the soft layer in Cases 1 and 2. This result indicates that even under the same bedding orientation, the crack initiation and propagation can be influenced by the volume fractions of different materials. To some extent, the phase field method naturally captures the various crack patterns from different configurations of the layered system.

Finally, we compare the bulk energies of Cases 1–3 with different layer orientations in Figure 11. Regardless of the volume fraction changes, the maximum bulk energies are obtained when the layers are aligned

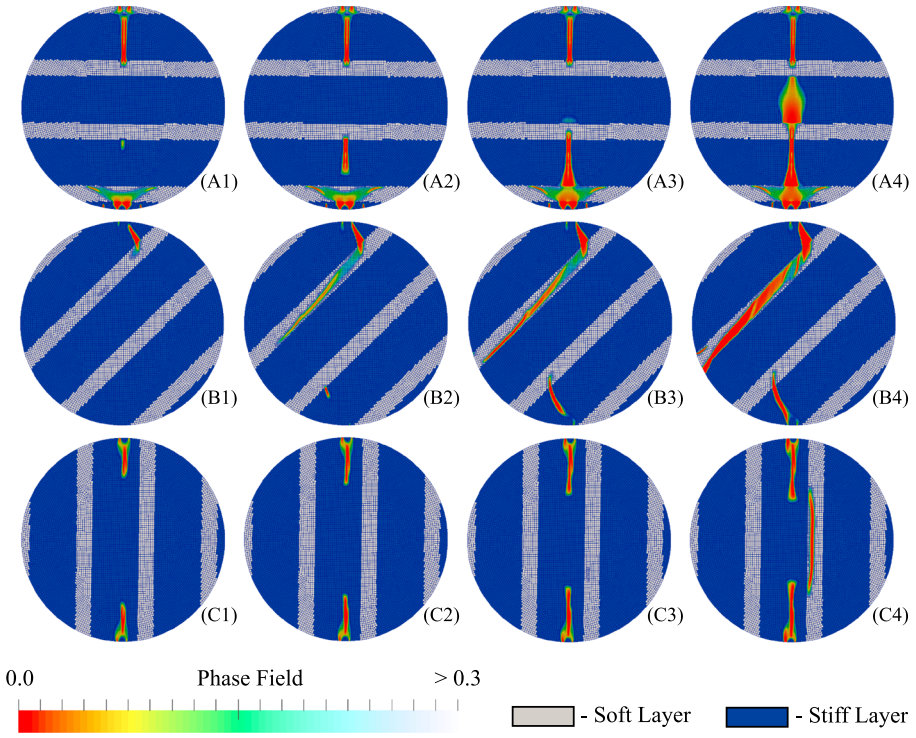

Figure 9. Sequence of crack propagation in Case 2 (stiff: 75.0%; soft: 25.0%) for each orientation of layers: (a) horizontal layer, (b) inclined layer, and (c) vertical layer. The range of phase field from 0.0 to 0.3 is selected for visualization purpose to highlight fracture patterns over the layered domain. Young's moduli of stiff and soft layers are 70.0 and 5.6 GPa, respectively.

perpendicular to the loading direction (horizontal layer). When we change the volume fraction by fixing the orientation, the maximum bulk energies of each case show little difference. Overall, this comparison reveals that the volume fraction of stiff layers from 40.5% to 75.0% has little impact on the maximum crack propagation energy when the explicit orientation of layers exists. Within the given range of volume fraction, therefore, the variation of layer orientations is more influential on the effective fracture toughness than the change of material compositions.

3.2.4. Case 4: Influence of Layer Thickness on Fracture Patterns

The thickness of each layer is reduced by increasing the number of layers to maintain the same volume fraction of stiff and soft layers. This treatment is applied to Case 4 based on Case 1 as a reference (see Table 2 for the case description). A comparison of crack patterns between Cases 1 and 4 for all orientations (Figures 6(A1) to 6(A4) and 12(A1) to 12(A4)) shows that the layer thickness and geometrical configurations of stiff and soft layers significantly affect crack propagation patterns. In the horizontal layer, for example, the direction of the main crack propagation in Case 4 is reversed from upward (i.e., bottom to top) to downward compared to Case 1. This indicates that the direction of crack propagations (i.e., upward or downward) is shifted due to the reduced layer thickness, though the same volume fractions of stiff and soft constituents are preserved. The change of layer thickness alters the location and arrangement of stiff and soft layers against the loading points, which contributes to the spatial elastic heterogeneity in the specimen.

For the inclined layer (45°), the main crack in the upper region moves to the outer boundary of the domain within a very narrow soft layer. The onset of the crack around the bottom part, however, is hardly initiated, which shows that the location and thickness of the soft and stiff layers against the loading contacts alter the crack propagation significantly. For the vertical layer (0°), the crack vertically propagates through the soft layer, as the increasing number of layers leads one of the soft layers to be located around the centerline. These results are further analyzed through the comparison of bulk energy. The role of weak materials such as defects on the fracture patterns and the effective fracture toughness is further explored in section 3.2.5.

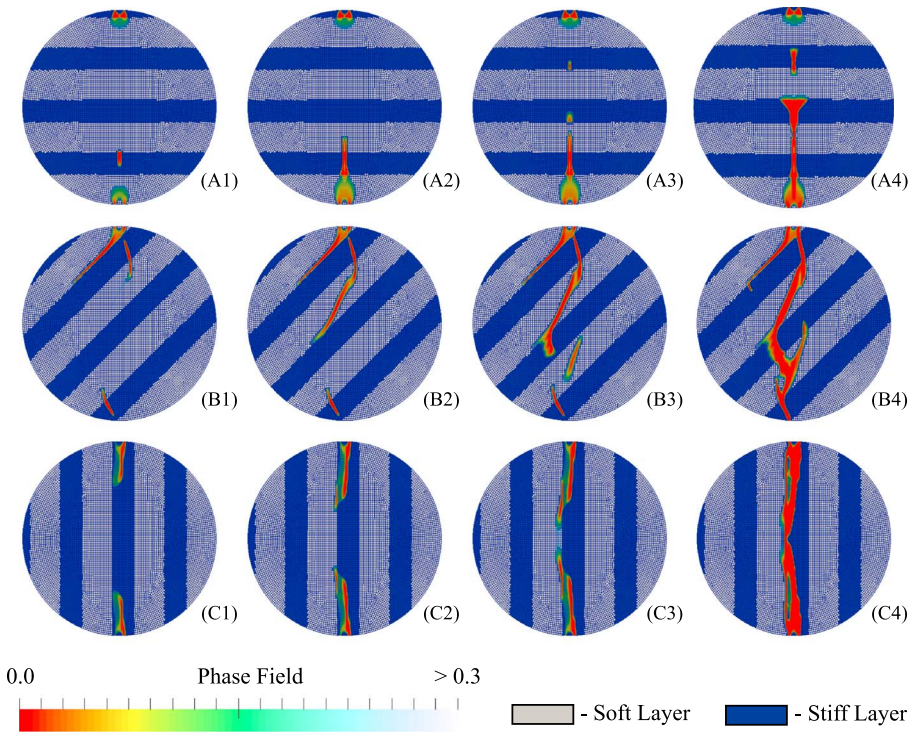

Figure 10. Sequence of crack propagation in Case 3 (stiff: 40.5%; soft: 59.5%) for each orientation of layers: (a) horizontal layer, (b) inclined layer, and (c) vertical layer. The range of phase field from 0.0 to 0.3 is selected for visualization purpose to highlight fracture patterns over the layered domain. Young's moduli of stiff and soft layers are 70.0 and 5.6 GPa, respectively.

The bulk energies of Cases 1 and 4 are presented in Figure 13. Compared to the horizontal layer condition, the bulk energies from inclined and vertical bedding conditions are significantly diminished in Case 4. As seen in Figure 12, the main cracks in the inclined and vertical layers initiate and propagate along the soft layer due to the geometrical changes of layers against the loading contacts. This results in reducing the effective fracture toughness or the material strength. Note that the effective fracture toughness is closely related to the maximum macroscopic energy release rate, which can be expressed by the bulk energy of the whole domain of heterogeneous material [*Hossain et al*., 2014]. The analysis of Case 4 indicates that the layer thickness changes of the layered material highly affect the effective fracture toughness under the Brazilian test condition.

3.2.5. Case 5: Influence of Elastic Heterogeneity on Macroscopic Crack Propagation

The effect of mesoscale heterogeneity, such as defects in the layered system, is investigated in Case 5 by introducing discontinuity into the stiff layers. Two different patterns in Figure 14 are designed based on Case 4 with horizontal layers. We embedded the soft layer in each stiff layer by replacing 1 mm thick of

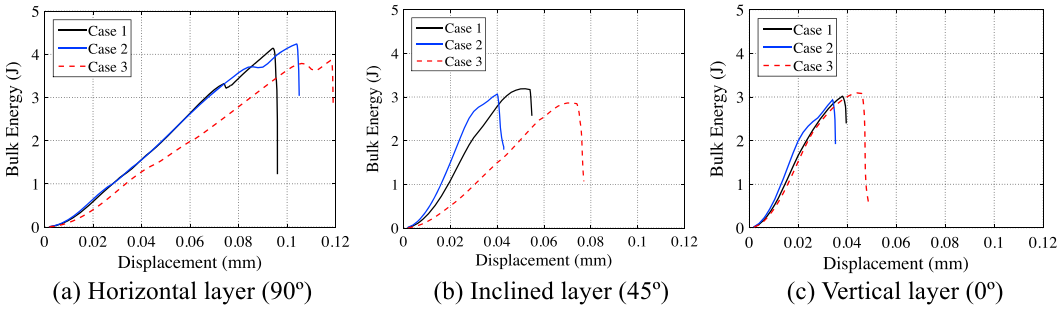

Figure 11. Comparison of bulk energies with different volume fractions (Case 1 (stiff: 62.6%; soft: 37.4%), Case 2 (stiff: 75.0%; soft: 25.0%), and Case 3 (stiff: 40.5%; soft: 59.5%)) in three different orientations with respect to the loading direction. (a) 90°, (b) 45°, and (c) 0°.

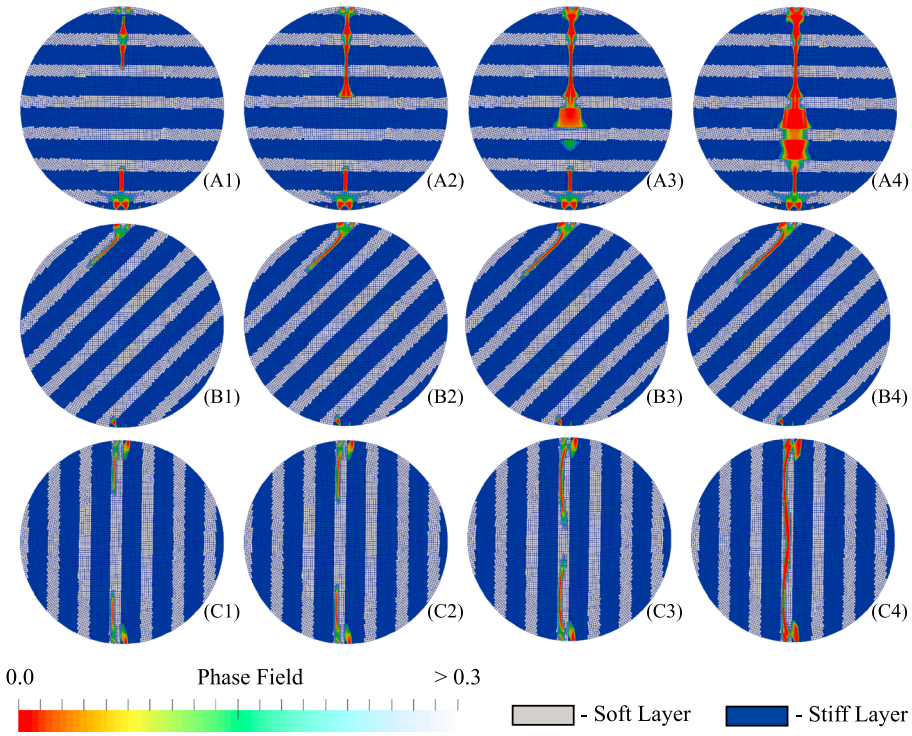

Figure 12. Sequence of crack propagation in Case 4 for each orientation of layers: (a) horizontal layer, (b) inclined layer, and (c) vertical layer). Case 4 has the same volume fraction of each constituent as Case 1 but has a thinner layer thickness. The range of phase field from 0.0 to 0.3 is selected for visualization purpose to highlight fracture patterns over the layered domain. Young's moduli of stiff and soft layers are 70.0 and 5.6 GPa, respectively.

the stiff layer with the soft constituent. Following the vertical centerline, the gaps are misaligned by 2 and 4 mm for Patterns 1 and 2, respectively. The simulation results show that the mesoscale heterogeneity affects the crack propagation [cf. *Hossain et al*., 2014] significantly. Without the discontinuity (Figure 12), the major crack develops vertically through the central region when the layers are horizontal (90°). For Pattern 1, multiple cracks simultaneously initiate around each discontinuity and coalesce to a major crack that meanders through the soft layers. For Pattern 2, the cracks do not follow the soft layer only. Instead, the cracks not only break through the stiff layers but branch and merge while propagating. In addition, the maximum bulk energy in Pattern 2 is higher than in other cases, even though the volume fraction of the stiff component is decreased and multiple defects in the stiff layer exist (Figure 15). This clearly demonstrates that elastic heterogeneity strongly influences effective fracture toughness and the crack path. With respect to the

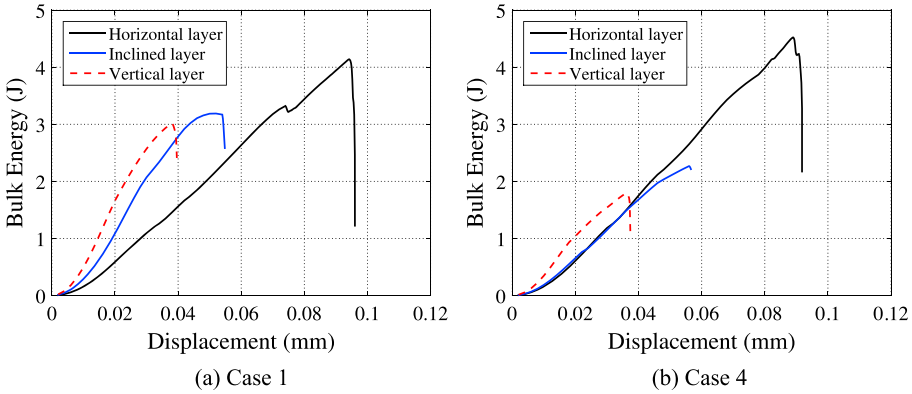

Figure 13. Comparison of bulk energies with different bedding orientations for (a) Case 1 and (b) Case 4. Case 4 has the same volume fraction of each constituent as Case 1 but has a thinner layer thickness. Layer configurations are shown in Figures 6 and 12.

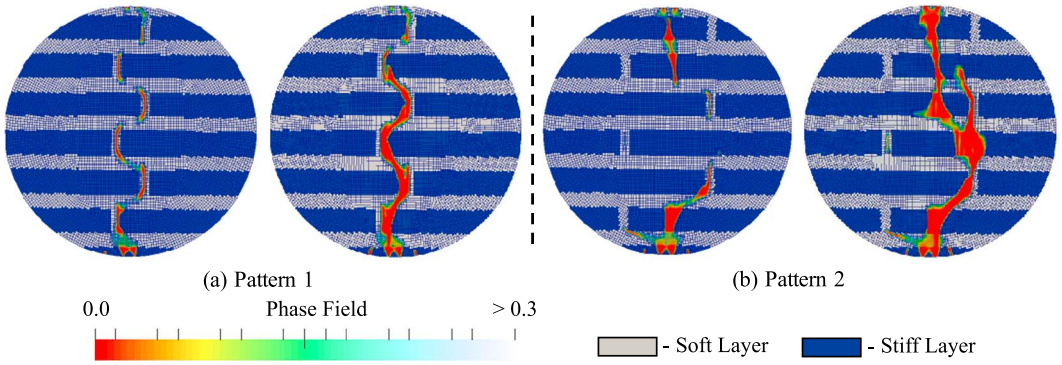

Figure 14. Crack propagation patterns under the existing defects in stiff layers (Case 5). The range of phase field from 0.0 to 0.3 is selected for visualization purpose. The width of defect in the stiff layer is 2 mm. Patterns (a) 1 and (b) 2 have the defect misaligned from the centerline of the domain by 2 and 4 mm, respectively. Young's moduli of stiff and soft layers are 70.0 and 5.6 GPa, respectively.

composition of layers, this example further shows the important role of soft layers in the fracture behavior (cf. section 3.2.4).

As observed in simulations and experimental results, the material heterogeneity (e.g., high clay regions) and existing flaws can strongly influence the onset and propagation of cracks. *Lanaro et al*. [2009] demonstrates that the stress induced by the existing cracks during the Brazilian test was much higher at the bridges between the cracks than that of direct tensile tests. More recently, *Li and Wong* [2013] derived a simple critical extension strain criterion for crack initiation and propagation on the Brazilian disk surface based on *Stacey*'s [1981] assumption (i.e., ideal linear deformation behavior), in which the intermediate principal stress was neglected. According to the formula in *Li and Wong* [2013], the required tensile stress for the soft component of Mancos Shale (e.g., Young's modulus = 10–20 MPa and Poisson's ratio = 0.2–0.3) is less than 1 MPa, which is much lower than the apparent tensile strength of Mancos Shale. The development of the tensile stress field in experimental samples A and B may be attributed to the distribution of weak materials (e.g., clay) and possibly existing cracks.

3.2.6. Case 6: Implications for Upscaling the Effective Properties of Heterogeneous Geomaterials

In this section, the transversely isotropic effective medium is obtained by the homogenization procedure [*Berryman*, 1998] based on the layered system of Case 1. The crack propagation patterns (Figure 16) reveal that the spatial homogenization procedure, if only applied to the elasticity material parameters, may lead to much simpler crack patterns than those from the layered isotropic materials. Interestingly, the transversely isotropic model for the inclined layer shows a slightly tilted crack topology around the center of the domain. This is geometrically much simpler than the experimental (Figure 5) and simulated (Figure 6) fracture patterns.

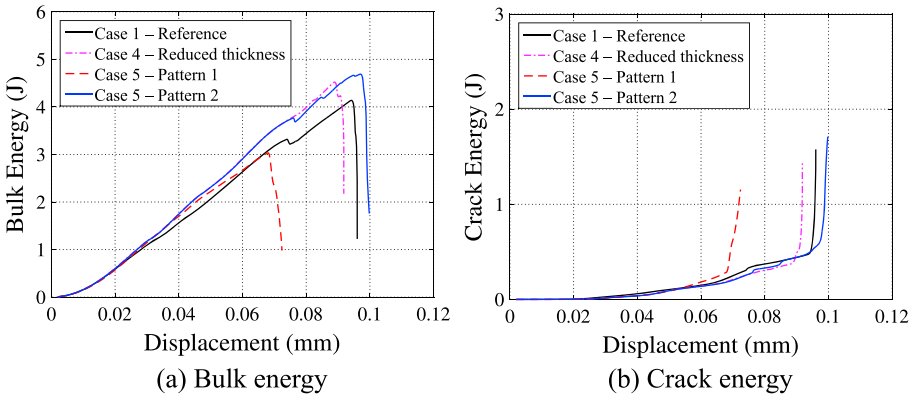

Figure 15. Comparison of bulk and crack energies for the effect of spatial heterogeneity in elastic features. The relevant configurations are corresponding to Figure 6 (Case 1—Original), Figure 12 (Case 1), Figure 12 (Case 4), and Figure 14 (Case 5 with Patterns 1 and 2).

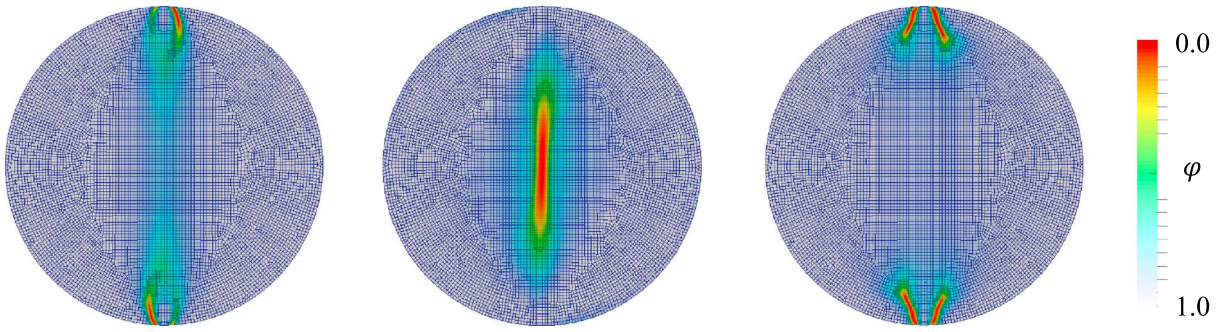

Figure 16. Crack patterns in the transverse isotropic effective medium (Case 6) for different orientations. The φ indicates the phase field for diffusive crack topology. The crack patterns can be compared to the explicit layer conditions (with the same volume fraction) in Figures 6 (Case 1) and 12 (Case 4).

The homogenization may filter out mesoscopic information; hence, the crack paths in the effective medium tend to be less tortuous. As a result, the smaller surface area created by the fracture process yields the reduced tortuous crack paths with a diminished amount of energy dissipation. Therefore, the effective medium may appear much tougher than the heterogeneous counterpart, as it has lost all the fast pathways that allow cracks to develop at low energy costs. Figure 17a shows that the maximum bulk energies obtained from the effective media are much higher than those observed in the three orientation layers of Case 1 (Figure 8a). Consequently, the homogenization procedure is likely to overestimate the effective fracture toughness. The fracture patterns and the resultant energy dissipation of the heterogeneous materials with mesoscopic features (e.g., layers and defects), as well as the transversely isotropic effective medium generated from the homogenization procedure are profoundly different.

3.2.7. Case 7: Effect of Anisotropy of Soft Layer on Crack Propagation

We idealize the soft layer as a linear elastic transverse isotropic material, in which the rotational axis of symmetry is perpendicular to the bedding or thin lamination (Case 7). The material properties used in the simulations are listed in Table 3. Note that this simplified setting is not sufficient to replicate the complex microstructural attributes of the real shale specimen. Nevertheless, this parametric study may provide insight on how anisotropy of individual layers affects the macroscopic responses. In this study, six numerical simulations are conducted with three different layer orientations and two types of layer thickness (as in Cases 1 and 4). The simulation results are shown in Figures 18a–18c and 18d–18f, which correspond to Figures 6(A4), 6(B4), and 6(C4), and 12(A4), 12(B4), and 12(C4), respectively. For the horizontal and inclined layers, the major cracks in Case 7 tend to be less developed in the anisotropic soft layer, compared to Cases 1 and 4. For the vertical layer, the crack propagations in Case 7 show very similar patterns to those in Cases 1 and 4. This may indicate

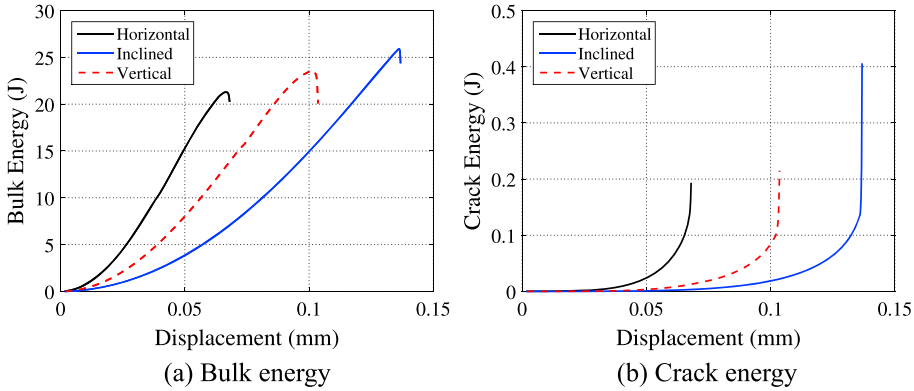

Figure 17. Comparison of bulk and crack energies (Case 6 with transversely isotropic effective medium conditions). Crack patterns of Case 6 are shown in Figure 16. The bulk energies can be compared to the explicit layer conditions (with the same volume fraction) in Figure 13 (Cases 1 and 4).

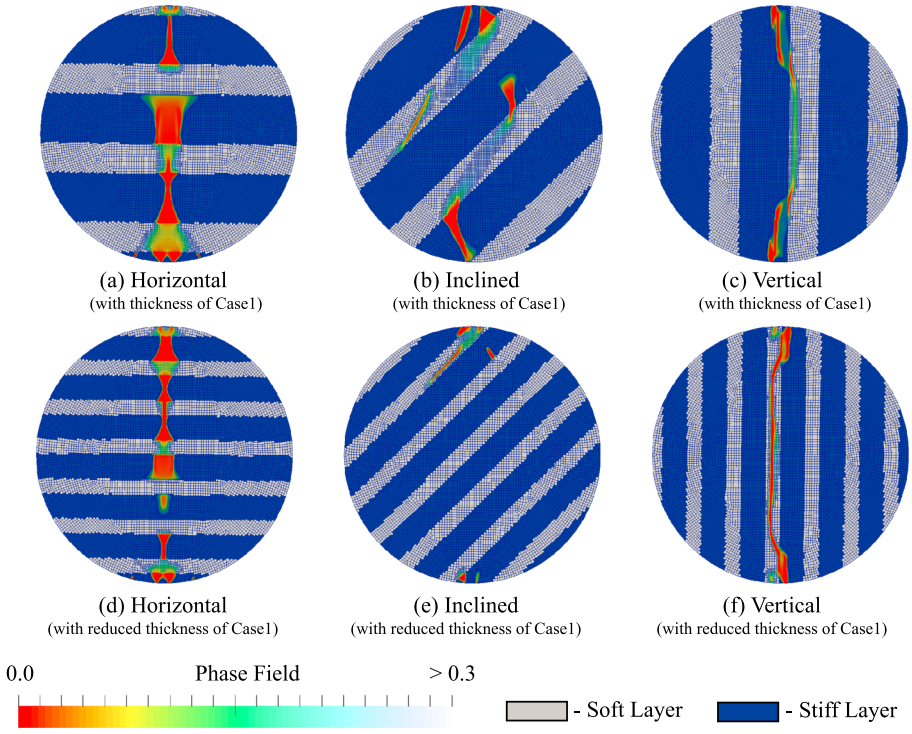

Figure 18. Crack propagation patterns (Case 7) with isotropic stiff and anisotropic soft layers for three different layer orientations. (a–c) Thicker layers and (d–f) thinner layers. Elastic properties of stiff and soft layers are in Table 3. The range of phase field from 0.0 to 0.3 is selected for visualization purpose. The crack patterns with isotropic stiff and soft layers are shown in Figures 6 and 12.

that fracture intersection with bedding layers is strongly related to the anisotropic properties in this particular configuration. Note that the elastic property in the soft layer is weaker perpendicular than parallel to the bedding. The phase field distribution shows that cracks are not fully developed across the soft layer when the loading direction is not aligned to the bedding direction. Due to the higher Young's modulus (E_1) along the bedding plane, the tensional crack is limited to propagate though the bedding layer. Instead, the damage zone becomes wider at the interface of the bedding. On the other hand, the crack easily propagates along the bedding direction for the vertical layer (Figures 18c and 18f).

The bulk energies in Case 7 are further compared with Cases 1 and 4 in Figure 19. Interestingly, the maximum bulk energy increases with increasing the angle between the bedding and loading directions

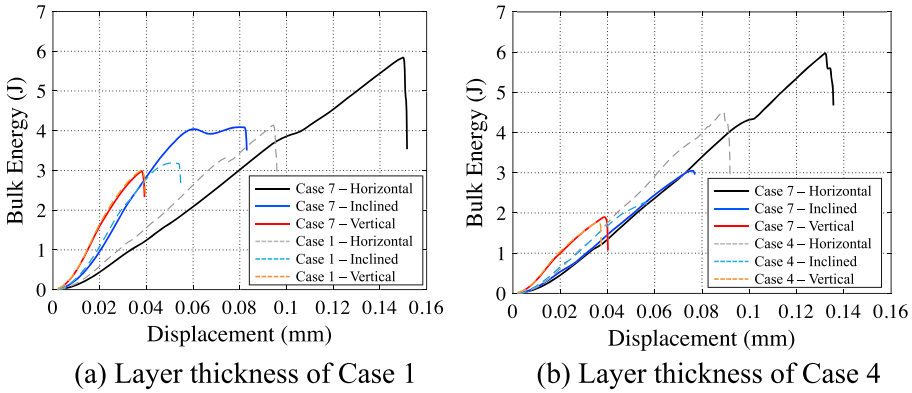

Figure 19. Comparison of bulk energies for different layer thicknesses (Case 7). (a) Case 7 with the layer thickness of Case 1 and (b) Case 7 with the layer thickness of Case 4. For Case 7 the stiff and soft layers are isotropic and transverse isotropic materials, respectively. The solid and dashed lines correspond to Cases 7 and 1 (or 4), respectively.

for both Cases 1 and 7. As seen in the phase field distribution in Figure 18, failures also occur at a higher prescribed displacement in the order of the horizontal, inclined, and vertical layers. In other words, the specimen tends to undertake slightly more loading and deformation before the onset of brittle fracture. For Case 7 the elastic anisotropy of the soft layers, combined with the isotropic stiff layers, appears to be more influential when the bedding orientation is not aligned to the loading direction. In addition, the effective fracture toughness for the horizontal and inclined layers is higher in Case 7 than in Cases 1 and 4. Whether this conclusion can be further generalized to other sets of material parameters is unclear. Nevertheless, this comparison provides quantitative evidence of the potential impact of the mesoscale material property on the macroscopic behavior of shales such as fracture termination and propagation at bedding interfaces.

4. Summary and Conclusions

This study presents four experimental Brazilian tests with Mancos Shale specimens, as well as a series of comprehensive numerical studies motivated from the Brazilian test with a simple layered material. The initiation and propagation of cracks in four Mancos Shale specimens were estimated based on the strain distribution captured by digital image correlation. These observational results reveal that the local heterogeneity and the laminations against the loading direction significantly influence the characterization of crack patterns. Based on the experimental observations, numerical simulations using the phase field model are conducted to evaluate the brittle fracture processes under the various Brazilian test conditions. In particular, the laminated and intrinsically anisotropic shale is idealized as a two-constitutive composite consisting of stiff and soft bedding layers. In the series of numerical simulations, the phase field approach for fracture is proved to be efficient in simulating crack initiations and coalescence without additional criteria except for the inherent energy functional formulation. This robustness effectively captures multiple cracks under the spatially varying elastic heterogeneity. Our numerical simulations reveal that even under the assumption that two constituents exhibit the same fracture toughness, the macroscopic effective toughness is highly sensitive to the elasticity of the components and the geometrical features of the bedding.

Depending on the volume fraction, the orientation of the bedding concerning the loading direction, the geometrical attributes, and the thickness of the bedding layers, cracks may initiate, grow, and coalesce in many different ways. Phase field simulations using the highly idealized two-constituent systems may provide insights to account for the broad spectrum of fracture toughness of shales observed from the Brazilian test in the literature. By systematically varying the bedding orientation, the volume fractions of the constituents, the layer thickness, and the length of the bedding, our simulation results suggest that within the range of the material parameters used in this study, the orientations of layers with respect to the loading direction has a more significant impact on the effective fracture toughness than the volume fractions of the two constituents. The elastic material properties of layers, the spatial heterogeneity of defects, and the anisotropy of the bedding layers may all play a role in altering the fracture patterns, therefore affecting the effective fracture toughness under the idealized conditions during the Brazilian test. Simulation results also suggest that a proper incorporation of additional material information, such as bedding layer thickness and other geometrical attributes of the microstructures, may yield improvements on the numerical predictions of the mesoscale fracture pattern and hence the macroscopic effective toughness.

By using multiscale experimental techniques to extract microstructural information and material properties of shale, one may be able to predict the exact location of each constituent in the shale to further improve the numerical simulations. It should be noted that the numerical simulations conducted in this study are based on a highly idealized setting for the Brazilian test. In a more realistic setting, compositional heterogeneity, texture and mineralogical orientations, and mechanical anisotropy need to be included properly. Furthermore, the hydro-mechanical coupling and nonlinear responses such as plasticity and creeping need to be considered in future research. For engineering applications such as geological CO_2 storage and hydraulic fracturing, a more comprehensive consideration of environmental factors, including thermal expansion of constituents, reactive transport in the void space, and the mechanical and chemical fluid-rocks interactions, must be taken into account for predicting fracture behaviors. These factors are out of the scope of this study but will be examined in future study.

Appendix A: Material Parameter Sensitivity in a Homogenized Effective Medium

This section presents the sensitivity analysis of the constitutive responses of the isotropic effective medium with material properties. The objectives of the sensitivity analysis using the isotropic material are to (1) ensure that our numerical code is correctly implemented to match the analytical solutions in the benchmark problem with a linear isotropic elastic material and (2) demonstrate that the mechanical responses from the Brazilian test simulations are consistent with expected behaviors when material parameters are varied in the idealized isotropic case. The isotropic effective medium is assumed to exhibit the following mechanical properties: Young's modulus is set at 20.0 GPa, and Poisson's ratio is set at 0.2. A cylinder domain with a radius (R) of 13.0 mm is discretized to represent the specimen in the Brazilian test experiment setup.

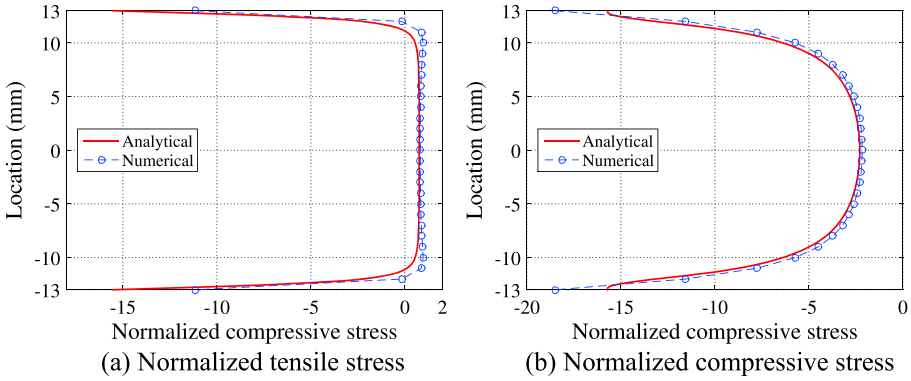

Figure A1. (a) Normalized tensile and (b) compressive stress distributions in a circular domain in the Brazilian test obtained from analytical solution and numerical simulation.

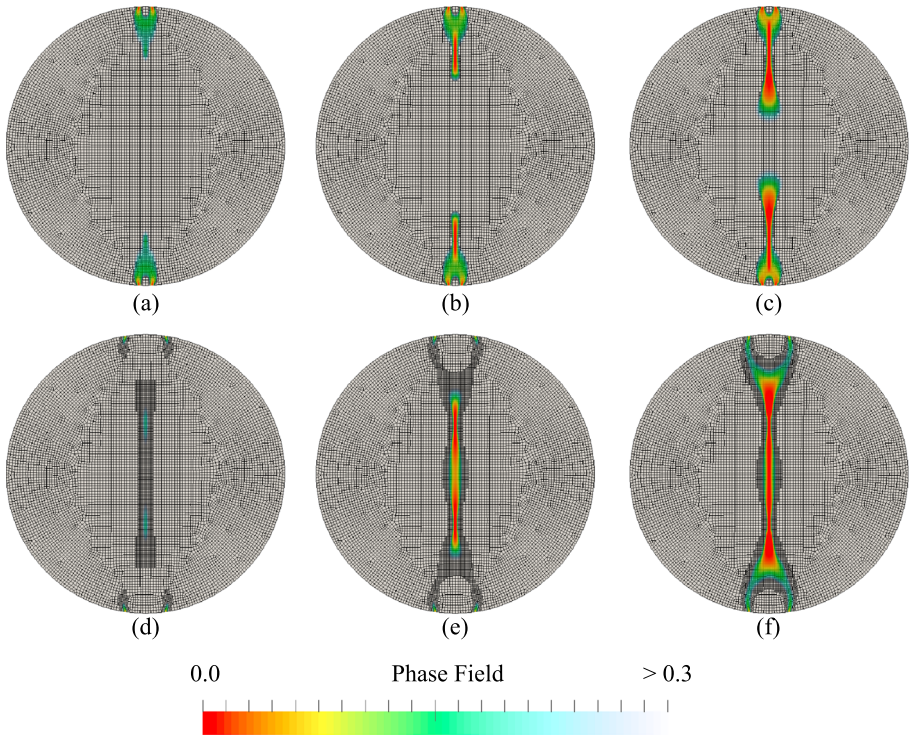

Figure A2. Comparison of crack propagations with different angular distributions of loading (i.e., loading angle) in the homogeneous domain (see Figure 3 for the schematic of angular distribution of loading). (a–c) Loading angle of 5.0° and (d–f) loading angle of 17.5°. The range of phase field from 0.0 to 0.3 is selected for visualization purpose to highlight fracture patterns over the domain.

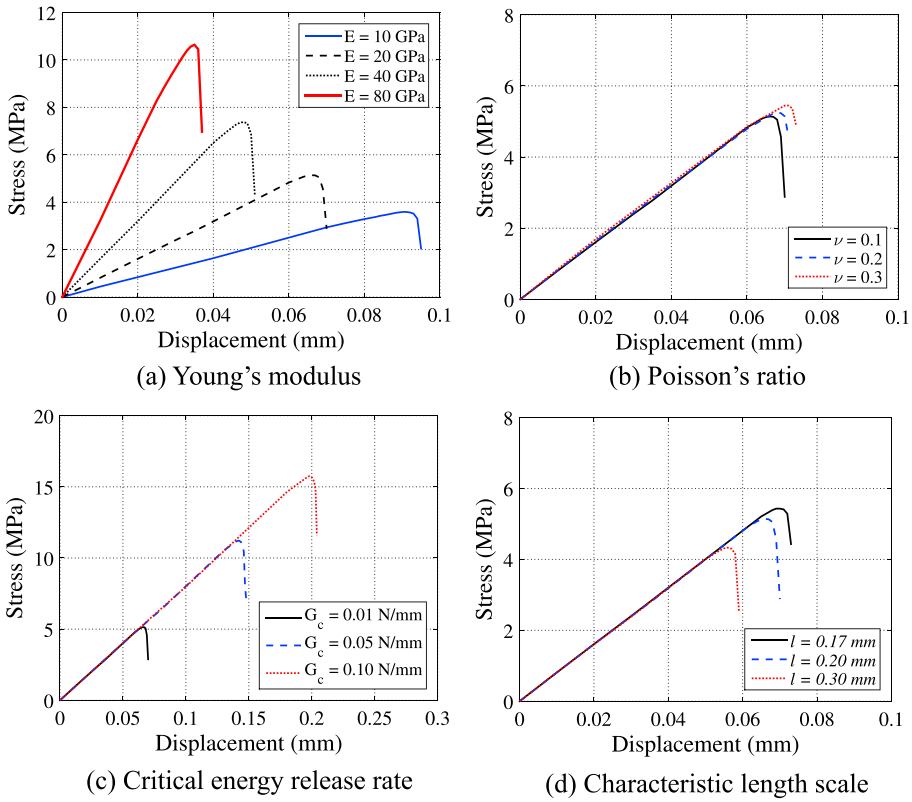

Figure A3. Stress-axial displacement results for sensitivity analysis of (a) Young's modulus, (b) Poisson's ratio, (c) critical energy release rate, and (d) characteristic length scale (cf. Table A1).

First, we validate the numerical model by checking whether the normalized stress distribution is consistent with the analytical solution from *Hondros* [1959]. The analytical solution is obtained by assuming that the material is homogeneous, isotropic, and linearly elastic. The stress distribution along the vertical central axis of a thin disc-shaped specimen is obtained, under which a uniform traction is applied on the top of the specimen with an equal and opposite reaction traction at the bottom [*Hondros*, 1959]. In Figure A1, the stress is normalized by dividing $P/\pi Rt$, in which P is the applied load and t is the unit thickness for two-dimensional condition. The tensile and compressive stress distributions along the central axis from the numerical simulation show good agreement with the analytical results.

In addition, we evaluate the influence of the loading contact area on the crack pattern. In the ASTM standard Brazilian test, the tensile strength of the specimen is estimated based on the assumptions that (1) the crack initiates from the central part of the disc, (2) the specimen is assumed homogeneous and isotropic, and (3) the constitutive response of the specimen is linearly elastic until the crack begins to propagate [e.g., *Hondros*, 1959; *Fairhurst*, 1964]. The crack, however, may initiate away from the center depending on the loading boundary condition, which may induce stress concentration around the contact area [cf. *Andreev*, 1991a]. Figure A2 shows the crack patterns generated from two loading cases where the two central angles (θ is defined in Figure 3) are 5.0° and 17.5°. The comparison demonstrates that the crack initiates near the

Table A1. Parameter Values for Sensitivity Analysis

Parameter	Description	Values	Unit
E	Young's modulus	10.0, 20.0, 40.0, 80.0	GPa
ν	Poisson's ratio	0.1, 0.2, 0.3	–
G_c	Critical energy release rate	0.01, 0.05, 0.10	N/mm
l	Characteristic length	0.17, 0.20, 0.30	mm

loading contact area when θ is 5° but initiates near the center of the specimen when the contact area is larger (θ = 17.5°). This result indicates that the location of crack initiation depends strongly on the contact area between the specimen and the loading platen, and the types of boundary conditions applied on the specimen. This finding is consistent with *Hudson et al*. [1972] and the follow-up discussion by *Datta* [1973]. Their research revealed that the location of crack initiation is influenced by the type of loading applied on the platen and that stress concentration may lead to cracks initiating under the contact area.

Finally, we evaluate the sensitivity of selected material properties by changing the input values for numerical simulation. The ranges of input values of numerical model are presented in Table A1, and simulation results are shown in Figure A3. Note that Young's modulus (E) and Poisson's ratio (ν) define the elastic properties of isotropic homogeneous materials while the critical energy release rate (G_c) is the material's resistance to fracture. Furthermore, different characteristic length scales (l) were selected to evaluate the influence of the regularization parameter on the simulation result.

As stated, G_c indicates the crack resistance, which is related to fracture toughness. This physical parameter implies that the higher the critical energy release rate, the more energy is required for crack propagation. This trend can be identified from the area below the stress-displacement curve in Figure A3c. In addition, how the characteristic length scale (l) influences the strength of homogeneous materials is analyzed. In the phase field model, the crack is not represented by strong discontinuity but by an implicit function. A diffusive crack may turn into sharp topology when the length scale l approaches to 0. The numerical simulations show that the smaller value of l leads the higher strain energy and tensile stress to trigger the crack, as previously reported in *Miehe et al*. [2010a].

Acknowledgments

This work was supported by the Laboratory Directed Research and Development program at Sandia National Laboratories, the Earth Materials and Processes program at the U.S. Army Research Office under grant contracts W911NF-14-1-0658 and W911NF-15-1-0581, and the Mechanics of Material program at National Science Foundation under grant contracts CMMI-1462760 and EAR-1516300. Brazilian tests and experimental analysis were supported from the U.S. Department of Energy, the Office of Science, Basic Energy Sciences under award DE-SC0006883. These supports are gratefully acknowledged. The authors are grateful to the developers of deal.II for valuable information and assistance in the finite element implementation and analysis. Sandia National Laboratories is a multimission laboratory managed and operated by National Technology and Engineering Solutions of Sandia, LLC., a wholly owned subsidiary of Honeywell International, Inc. for the U.S. Department of Energy's National Nuclear Security Administration under contract DE-NA-0003525. We also acknowledge the effort of the Associate Editor and two anonymous reviewers for their careful and constructive reviews, which led to tremendous improvement of our manuscript. The data for this paper are available by contacting the corresponding author (Hongkyu Yoon) at hyoon@sandia.gov.

References

Amadei, B. (1996), Importance of anisotropy when estimating and measuring in situ stresses in rock, *Int. J. Rock Mech. Min. Sci. Geomech. Abstr.*, *33*(3), 293–325.

Ambati, M., T. Gerasimov, and L. De Lorenzis (2015), Phase-field modeling of ductile fracture, *Comput. Mech.*, *55*(5), 1017–1040.

An, H., J. Shi, X. Zheng, and X. Wang (2016), Hybrid finite-discrete element method modeling of rock failure processes in brazilian disc tests, *Electron. J. Geotech. Eng.*, *21*(7).

Anderson, T. L. (2005), *Fracture Mechanics: Fundamentals and Applications*, Taylor and Francis, Boca Raton, Fla.

Andreev, G. (1991a), A review of the brazilian test for rock tensile strength determination. Part I: Calculation formula, *Min. Sci. Technol.*, *13*(3), 445–456.

Andreev, G. (1991b), A review of the brazilian test for rock tensile strength determination. Part II: Contact conditions, *Min. Sci. Technol.*, *13*(3), 457–465.

ASTM (2008) *Standard Test Method for Splitting Tensile Strength of Intact Rock Core Specimens (astm d3967-08)*, Standard, ASTM Int., West Conshohocken, Pa.

Backus, G. E. (1962), Long-wave elastic anisotropy produced by horizontal layering, *J. Geophys. Res.*, *67*(11), 4427–4440.

Bangerth, W., R. Hartmann, and G. Kanschat (2007), deal.II a general-purpose object-oriented finite element library, *ACM Trans. Math. Soft. (TOMS)*, *33*(4), 24.

Bangerth, W., T. Heister, L. Heltai, G. Kanschat, M. Kronbichler, M. Maier, B. Turcksin, and T. Young (2013), The deal.II library, version, 8, 1–5.

Berryman, J. G. (1998), Transversely isotropic poroelasticity arising from thin isotropic layers, in *Mathematics of Multiscale Materials*, pp. 37–50, Springer, New York.

Blatt, H., R. Tracy, and B. Owens (2006), *Petrology: Igneous, Sedimentary, and Metamorphic*, W.H. Freeman, New York.

Borden, M. J., C. V. Verhoosel, M. A. Scott, T. J. Hughes, and C. M. Landis (2012), A phase-field description of dynamic brittle fracture, *Comput. Methods Appl. Mech. Eng.*, *217*, 77–95.

Bourdin, B., G. A. Francfort, and J.-J. Marigo (2008), The variational approach to fracture, *J. Elast.*, *91*(1–3), 5–148.

Burstedde, C., L. Wilcox, and O. Ghattas (2011), p4est: Scalable algorithms for parallel adaptive mesh refinement on forests of octrees, *SIAM J. Sci. Comput.*, *33*(3), 1103–1133.

Chandler, M. R., P. G. Meredith, N. Brantut, and B. R. Crawford (2016), Fracture toughness anisotropy in shale, *J. Geophys. Res. Solid Earth*, *121*, 1706–1729, doi:10.1002/2015JB012756.

Chen, C.-S., E. Pan, and B. Amadei (1998), Determination of deformability and tensile strength of anisotropic rock using brazilian tests, *Int. J. Rock Mech. Min. Sci.*, *35*(1), 43–61.

Cholach, P. Y., and D. R. Schmitt (2006), Intrinsic elasticity of a textured transversely isotropic muscovite aggregate: Comparisons to the seismic anisotropy of schists and shales, *J. Geophys. Res.*, *111*, B09410, doi:10.1029/2005JB004158.

Chong, K., J. Chen, G. Dana, and J. Weber (1984), Indirect and direct tensile behavior of devonian oil shales, *Tech. Rep., DOE/LC/10877-1567 ON: DE84009296*, Wyoming Univ., Dep. of Civ. Eng., Laramie, Wyo.

Choo, J., and R. I. Borja (2015), Stabilized mixed finite elements for deformable porous media with double porosity, *Comput. Methods Appl. Mech. Eng.*, *293*, 131–154.

Choo, J., J. A. White, and R. I. Borja (2016), Hydromechanical modeling of unsaturated flow in double porosity media, *Int. J. Geomech.*, *16*(6) D4016,002.

Claesson, J., and B. Bohloli (2002), Brazilian test: Stress field and tensile strength of anisotropic rocks using an analytical solution, *Int. J. Rock Mech. Min. Sci.*, *39*(8), 991–1004.

Dan, D. Q., and H. Konietzky (2014), Numerical simulations and interpretations of brazilian tensile tests on transversely isotropic rocks, *Int. J. Rock Mech. Min. Sci.*, *71*, 53–63.

Dan, D. Q., H. Konietzky, and M. Herbst (2013), Brazilian tensile strength tests on some anisotropic rocks, *Int. J. Rock Mech. Min. Sci.*, *58*, 1–7.

Datta, R. N. (1973), The controlled failure of rock discs and rings loaded in diametral compression: Contribution to discussion of the paper by J.A. Hudson et al. 1972, *Int. J. Rock Mech. Min. Sci. Geomech. Abstr.*, *10*(3), 247–249.
Debasis, D., and V. A. Kumar (2016), *Fundamentals and Applications of Rock Mechanics*, PHI Learning Pvt. Ltd, New Delhi, India.
Dolbow, J., N. Moës, and T. Belytschko (2000), Discontinuous enrichment in finite elements with a partition of unity method, *Finite Elem. Anal. Des.*, *36*(3), 235–260.
Eftekhari, M., A. Baghbanan, and H. Hashemolhosseini (2015), Extended finite element simulation of crack propagation in cracked brazilian disc, *J. Mining Environ.*, *6*(1), 95–102.
Erarslan, N., and D. J. Williams (2012), Experimental, numerical and analytical studies on tensile strength of rocks, *Int. J. Rock Mech. Min. Sci.*, *49*, 21–30.
Exadaktylos, G., and K. Kaklis (2001), Applications of an explicit solution for the transversely isotropic circular disc compressed diametrically, *Int. J. Rock Mech. Min. Sci.*, *38*(2), 227–243.
Fairhurst, C. (1964), On the validity of the 'Brazilian' test for brittle materials, *Int. J. Rock Mech. Min. Sci. Geomech. Abstr.*, *1*(4), 535–546.
Folk, R. L. (1980), *Petrology of Sedimentary Rocks*, Hemphill Co., Austin.
Gercek, H. (2007), Poisson's ratio values for rocks, *Int. J. Rock Mech. Min. Sci.*, *44*(1), 1–13.
Gray, W. G., B. A. Schrefler, and F. Pesavento (2009), The solid phase stress tensor in porous media mechanics and the hill–mandel condition, *J. Mech. Phys. Solids*, *57*(3), 539–554.
Griffith, A. A. (1921), The phenomena of rupture and flow in solids, *Philos. Trans. R. Soc. London. Ser. A, Containing Pap. Math. Phys. Character*, *221*, 163–198.
Grigg, J. (2016), Influence of diagenetic minerals on the mechanical behavior of mudstones: Implications for natural and induced fracture development, Master's thesis, New Mexico Inst. of Min. and Technol., Socorro, N.M.
Guo, H., N. Aziz, and L. Schmidt (1993), Rock fracture-toughness determination by the brazilian test, *Eng. Geol.*, *33*(3), 177–188.
Hart, B. S., J. H. Macquaker, and K. G. Taylor (2013), Mudstone (shale) depositional and diagenetic processes: Implications for seismic analyses of source-rock reservoirs, *Interpretation*, *1*(1), B7–B26.
Heath, J. E., T. A. Dewers, B. J. McPherson, M. B. Nemer, and P. G. Kotula (2012), Pore-lining phases and capillary breakthrough pressure of mudstone caprocks: Sealing efficiency of geologic co 2 storage sites, *Int. J. Greenhouse Gas Control*, *11*, 204–220.
Heister, T., M. F. Wheeler, and T. Wick (2015), A primal-dual active set method and predictor-corrector mesh adaptivity for computing fracture propagation using a phase-field approach, *Comput. Methods Appl. Mech. Eng.*, *290*, 466–495.
Heroux, M., and J. Willenbring (2012), A new overview of the trilinos project, *Sci. Program.*, *20*(2), 83–88.
Hettinger, R. D., and M. A. Kirschbaum (2002), Stratigraphy of the upper cretaceous mancos shale (upper part) and mesaverde group in the southern part of the uinta and piceance basins, Utah and Colorado, *Tech. Rep.*, *I-2764*, U.S. Geol. Surv. (USGS). [Available at https://pubs.er.usgs.gov/publication/i2764.]
Hobbs, D. (1964), The tensile strength of rocks, *Int. J. Rock Mech. Min. Sci. Geomech. Abstr.*, *1*(3), 385–396.
Hofacker, M., and C. Miehe (2012), Continuum phase field modeling of dynamic fracture: Variational principles and staggered fe implementation, *Int. J. Fract.*, *178*(1–2), 113–129.
Hofacker, M., and C. Miehe (2013), A phase field model of dynamic fracture: Robust field updates for the analysis of complex crack patterns, *Int. J. Numer. Methods Eng.*, *93*(3), 276–301.
Hondros, G. (1959), The evaluation of poissons ratio and the modulus of materials of a low tensile resistance by the brazilian (indirect tensile) test with particular reference to concrete, *Aust. J. Appl. Sci.*, *10*(3), 243–268.
Hossain, M., C.-J. Hsueh, B. Bourdin, and K. Bhattacharya (2014), Effective toughness of heterogeneous media, *J. Mech. Phys. Solids*, *71*, 15–32.
Hudson, J. A., E.-F. Brown, and F. Rummel (1972), The controlled failure of rock discs and rings loaded in diametral compression, *Int. J. Rock Mech. Min. Sci. Geomech. Abstr.*, *9*(2), 241–248.
International Society of Rock Mechanics (1978), Suggested methods for determining tensile strength of rock materials, *Int. J. Rock Mech. Min. Sci. Geomech. Abstr.*, *15*(3), 99–103, doi:10.1016/0148-9062(78)90003-7.
Jaeger, J. C., N. G. Cook, and R. Zimmerman (2009), *Fundamentals of Rock Mechanics*, Blackwell, Malden, Mass.
Kaarsberg, E. A. (1959), Introductory studies of natural and artificial argillaceous aggregates by sound-propagation and x-ray diffraction methods, *J. Geol.*, 447–472.
Kauffman, E. G., W. Berggren, and J. Van Couvering (1984), The fabric of cretaceous marine extinctions, in *Catastrophes and Earth History: The New Uniformitarianism*, edited by W. A. Berggren and J. A. Van Couvering, pp. 151–246, Princeton Univ. Press, Princeton, N. J.
Kennedy, A. D. (2011), Geologic predictors of the hydrocarbon extraction potential of the mancos shale, Master's thesis, University of Utah.
Knudsen, O. Ø., A. Bjørgum, M. Polanco-Loria, A. Øyen, and R. Johnsen (2007), Internal stress and mechanical properties of paint films, in *CORROSION 2007*, Pap. No. 07003, NACE Int., Houston, Tex.
Kuhn, C., and R. Müller (2010), A continuum phase field model for fracture, *Eng. Fract. Mech.*, *77*(18), 3625–3634.
Kumar, V., C. H. Sondergeld, C. S. Rai, et al. (2012a), Nano to macro mechanical characterization of shale, in *SPE Annual Tech. Conf. and Exhibition*, SPE-159804-MS, Soc. of Petrol. Eng.
Kumar, V., et al. (2012b), Estimation of elastic properties of organic matter in woodford shale through nanoindentation measurements, in *SPE Canadian Unconventional Resour. Conf.*, SPE-162778-MS, Soc. of Petrol. Eng.
Lama, R., and V. Vutukuri (1978) *Handbook on Mechanical Properties of Rocks; Testing Techniques and Results*, *Series on Rock and Soil Mechanics 3*, vol. 1, Trans. Tech. Publ., Clausthal, Germany.
Lanaro, F., T. Sato, and O. Stephansson (2009), Microcrack modelling of brazilian tensile tests with the boundary element method, *Int. J. Rock Mech. Min. Sci.*, *46*(3), 450–461.
Landis, E. R., C. H. Dane, and W. A. Cobban (1973), Stratigraphic terminology of the dakota sandstone and mancos shale, west-central new mexico, *Tech. Rep., 1372-J*, U.S. Geol. Surv. (USGS). [Available at http://pubs.er.usgs.gov/publication/b1372J.]
Lazar, O. R., K. M. Bohacs, J. H. Macquaker, J. Schieber, and T. M. Demko (2015), Capturing key attributes of fine-grained sedimentary rocks in outcrops, cores, and thin sections: Nomenclature and description guidelines, *J. Sediment. Res.*, *85*(3), 230–246.
Lenoir, N., J. Andrade, W. Sun, and J. Rudnicki (2010), In situ permeability measurements inside compaction bands using X-ray CT and lattice boltzmann calculations, in *Advances in Computed Tomography for Geomaterials: GeoX2010*, edited by K. A. Alshibli and A. H. Reed, pp. 279–286, John Wiley, Hoboken, N. J.
Li, B., C. Peco, D. Millán, I. Arias, and M. Arroyo (2015), Phase-field modeling and simulation of fracture in brittle materials with strongly anisotropic surface energy, *Int. J. Numer. Methods Eng.*, *102*(3–4), 711–727.
Li, D., and L. N. Y. Wong (2013), The brazilian disc test for rock mechanics applications: Review and new insights, *Rock Mech. Rock. Eng.*, *46*(2), 269–287.

Loucks, R. G., R. M. Reed, S. C. Ruppel, and U. Hammes (2012), Spectrum of pore types and networks in mudrocks and a descriptive classification for matrix-related mudrock pores, *AAPG Bull.*, *96*(6), 1071–1098.
Mahabadi, O. K. (2012), Investigating the influence of micro-scale heterogeneity and microstructure on the failure and mechanical behaviour of geomaterials, PhD thesis, Univ. of Toronto.
Malan, D., J. Napier, and B. Watson (1994), Propagation of fractures from an interface in a brazilian test specimen, *Int. J. Rock Mech. Min. Sci. Geomech. Abstr.*, *31*(6), 581–596.
Miehe, C., M. Hofacker, and F. Welschinger (2010a), A phase field model for rate-independent crack propagation: Robust algorithmic implementation based on operator splits, *Comput. Methods Appl. Mech. Eng.*, *199*(45), 2765–2778.
Miehe, C., F. Welschinger, and M. Hofacker (2010b), Thermodynamically consistent phase-field models of fracture: Variational principles and multi-field fe implementations, *Int. J. Numer. Methods Eng.*, *83*(10), 1273–1311.
Mighani, S., C. Sondergeld, C. Rai (2014), Efficient completions in anisotropic shale gas formations, in Unconventional Resources Technology Conference (URTeC), URTeC-1934272, doi:10.15530/urtec-2014-1934272.
Mighani, S., C. H. Sondergeld, and C. S. Rai (2016), Observations of tensile fracturing of anisotropic rocks, *SPE J.*, SPE-1934272.
Moelans, N., B. Blanpain, and P. Wollants (2008), An introduction to phase-field modeling of microstructure evolution, *Calphad*, *32*(2), 268–294.
Mokhtari, M. (2015), Characterization of anisotropy in organic-rich shales: Shear and tensile failure, wave velocity, matrix and fracture permeability, PhD thesis, Colo. School of Mines, Golden.
Mota, A., J. Knap, and M. Ortiz (2008), Fracture and fragmentation of simplicial finite element meshes using graphs, *Int. J. Numer. Methods Eng.*, *73*(11), 1547–1570.
Na, S., and W. Sun (2017), Computational thermo-hydro-mechanics for multiphase freezing and thawing porous media in the finite deformation range, *Comput. Methods Appl. Mech. Eng.*, *318*, 667–700.
Nguyen, T. L., S. A. Hall, P. Vacher, and G. Viggiani (2011), Fracture mechanisms in soft rock: Identification and quantification of evolving displacement discontinuities by extended digital image correlation, *Tectonophysics*, *503*(1), 117–128.
Ong, O. N., D. R. Schmitt, R. S. Kofman, and K. Haug (2016), Static and dynamic pressure sensitivity anisotropy of a calcareous shale, *Geophys. Prospect.*, *64*(4), 875–897.
Park, B., and K.-B. Min (2015), Bonded-particle discrete element modeling of mechanical behavior of transversely isotropic rock, *Int. J. Rock Mech. Min. Sci.*, *76*, 243–255.
Park, B., et al. (2016), Three-dimensional bonded-particle discrete element modeling of transversely isotropic rock: Verification and application to laboratory test on shale, in *50th US Rock Mechanics/Geomechanics Symposium*, ARMA 16-160, Am. Rock Mech. Assoc.
Pasley, M. A., W. A. Gregory, and G. F. Hart (1991), Organic matter variations in transgressive and regressive shales, *Org. Geochem.*, *17*(4), 483–509.
Perras, M. A., and M. S. Diederichs (2014), A review of the tensile strength of rock: Concepts and testing, *Geotech. Geol. Eng.*, *32*(2), 525–546.
Pinto, J. (1979), Determination of the elastic constants of anisotropic bodies by diametral compression tests, in *4th ISRM Congress*, Int. Soc. for Rock Mech.
Reu, P. (2015), Points on paint, *Exp. Tech.*, *39*(4), 1–2.
Ridgley, J., S. Condon, and J. Hatch (2013), Geology and oil and gas assessment of the mancos-menefee composite total petroleum system: Chapter 4 in total petroleum systems and geologic assessment of undiscovered oil and gas resources in the san juan basin province, exclusive of paleozoic rocks, new mexico and Colorado, *Tech. Rep., 69-F-4*, U.S. Geol. Surv. (USGS). [Available at http://pubs.er.usgs.gov/publication/ds69F4.]
Salinger, A. G., et al. (2013), Albany: A component-based partial differential equation code built on trilinos., Tech. rep., Sandia National Laboratories Livermore, CA; Sandia National Laboratories (SNL-NM), Albuquerque, NM (United States).
Schlüter, A., A. Willenbücher, C. Kuhn, and R. Müller (2014), Phase field approximation of dynamic brittle fracture, *Comput. Mech.*, *54*(5), 1141–1161.
Shipton, Z. K., J. P. Evans, D. Kirschner, P. T. Kolesar, A. P. Williams, and J. Heath (2004), Analysis of co2 leakage through low-permeabilityfaults from natural reservoirs in the colorado plateau, east-central utah, *Geol. Soc. Lond., Spec. Publ.*, *233*(1), 43–58.
Simpson, N. D. J. (2013), An analysis of tensile strength, fracture initiation and propagation in anisotropic rock (gas shale) using brazilian tests equipped with high speed video and acoustic emission, Master's thesis, Norwegian University of Science and Technology.
Sondergeld, C. H., and C. S. Rai (2011), Elastic anisotropy of shales, *Lead. Edge*, *30*(3), 324–331.
Sone, H., and M. D. Zoback (2013a), Mechanical properties of shale-gas reservoir rockspart 1: Static and dynamic elastic properties and anisotropy, *Geophysics*, *78*(5), D381–D392.
Sone, H., and M. D. Zoback (2013b), Mechanical properties of shale-gas reservoir rockspart 2: Ductile creep, brittle strength, and their relation to the elastic modulus, *Geophysics*, *78*(5), D393–D402.
Stacey, T. (1981), A simple extension strain criterion for fracture of brittle rock, *Int. J. Rock Mech. Min. Sci. Geomech. Abstr.*, *18*(6), 469–474.
Sun, W., J. E. Andrade, J. W. Rudnicki, and P. Eichhubl (2011a), Connecting microstructural attributes and permeability from 3d tomographic images of in situ shear-enhanced compaction bands using multiscale computations, *Geophys. Res. Lett.*, *38*, L10302, doi:10.1029/2011GL047683.
Sun, W., J. E. Andrade, and J. W. Rudnicki (2011b), Multiscale method for characterization of porous microstructures and their impact on macroscopic effective permeability, *Int. J. Numer. Methods Eng.*, *88*(12), 1260–1279.
Sun, W., M. R. Kuhn, and J. W. Rudnicki (2013), A multiscale dem-lbm analysis on permeability evolutions inside a dilatant shear band, *Acta Geotech.*, *8*(5), 465–480.
Sutton, M. A., S. R. McNeill, J. D. Helm, and Y. J. Chao (2000), Advances in two-dimensional and three-dimensional computer vision, *Photomechanics*, *77*, 323–372.
Tan, X., H. Konietzky, T. Frühwirt, and D. Q. Dan (2015), Brazilian tests on transversely isotropic rocks: Laboratory testing and numerical simulations, *Rock Mech. RockEng.*, *48*(4), 1341–1351.
Tavallali, A., and A. Vervoort (2010a), Effect of layer orientation on the failure of layered sandstone under brazilian test conditions, *Int. J. Rock Mech. Min. Sci.*, *47*(2), 313–322.
Tavallali, A., and A. Vervoort (2010b), Failure of layered sandstone under brazilian test conditions: Effect of micro-scale parameters on macro-scale behaviour, *Rock Mech. Rock. Eng.*, *43*(5), 641–653.
Tavallali, A., and A. Vervoort (2013), Behaviour of layered sandstone under Brazilian test conditions: Layer orientation and shape effects, *J. Rock Mech. Geotech. Eng.*, *5*(5), 366–377.
Verhoosel, C. V., and R. Borst (2013), A phase-field model for cohesive fracture, *Int. J. Numer. Methods Eng.*, *96*(1), 43–62.
Vernik, L., and A. Nur (1992), Ultrasonic velocity and anisotropy of hydrocarbon source rocks, *Geophysics*, *57*(5), 727–735.

Vernik, L., and X. Liu (1997), Velocity anisotropy in shales: A petrophysical study, *Geophysics*, *62*(2), 521–532.
Vervoort, A., K.-B. Min, H. Konietzky, J.-W. Cho, B. Debecker, Q.-D. Dinh, T. Frühwirt, and A. Tavallali (2014), Failure of transversely isotropic rock under brazilian test conditions, *Int. J. Rock Mech. Min. Sci.*, *70*, 343–352.
Wang, J., L. Xie, H. Xie, L. Ren, B. He, C. Li, Z. Yang, and C. Gao (2016), Effect of layer orientation on acoustic emission characteristics of anisotropic shale in brazilian tests, *J. Nat. Gas Sci. Eng.*, doi:10.1016/j.jngse.2016.03.046.
White, J. A., and R. I. Borja (2008), Stabilized low-order finite elements for coupled solid-deformation/fluid-diffusion and their application to fault zone transients, *Comput. Methods Appl. Mech. Eng.*, *197*(49), 4353–4366.
White, J. A., and R. I. Borja (2011), Block-preconditioned newton–krylov solvers for fully coupled flow and geomechanics, *Comput. Geosci.*, *15*(4), 647–659.
Wick, T., G. Singh, and M. F. Wheeler (2015), Fluid-filled fracture propagation with a phase-field approach and coupling to a reservoir simulator, *SPE J.*, SPE-168597, doi:10.2118/168597-PA.
Yoon, H., et al. (2015), Multiscale characterization of physical, chemical, and mechanical heterogeneity of mudstones, in *49th US Rock Mechanics/Geomechanics Symposium*, ARMA 15-0463, Am. Rock Mech. Assoc.
Yu, Y., J. Yin, and Z. Zhong (2006), Shape effects in the brazilian tensile strength test and a 3d fem correction, *Int. J. Rock Mech. Min. Sci.*, *43*(4), 623–627.
Zhang, Z. J., and G. H. Paulino (2005), Cohesive zone modeling of dynamic failure in homogeneous and functionally graded materials, *Int. J. Plast.*, *21*(6), 1195–1254.
Zhu, W., and C. Tang (2006), Numerical simulation of brazilian disk rock failure under static and dynamic loading, *Int. J. Rock Mech. Min. Sci.*, *43*(2), 236–252.